NTNU

Norwegian University of
Science and Technology

Thrust Losses on Underwater Snake Robots with Thrusters

Mari Gilje Galta

Marine Technology
Submission date: August 2017
Supervisor: Asgeir Johan Sørensen, IMT
Co-supervisor: Eleni Kelasidi, ITK

Norwegian University of Science and Technology
Department of Marine Technology

NTNU
Norwegian University of
Science and Technology

MASTER THESIS IN MARINE CYBERNETICS

Summer 2017

for

STUD. TECH. Mari Gilje Galta

Study of Thrust Losses on Underwater Snake Robots with Thrusters

Work Description

NTNU is together with Eelume developing a disruptive solution for underwater inspection and maintenance in the form of a swimming robot. The idea is to let these robots do inspection and light intervention jobs on the seabed, reducing the use of large and expensive vessels. With its snake-like form, the slender and flexible body of the Eelume robot provides access to confined areas that are difficult to access with existing technology.

The project will study how much Eelume's underwater snake robot with thrusters is affected by thrust losses. Thrust losses focused on in this thesis are in-line velocity fluctuations, transverse velocity fluctuations, thruster-thruster interactions, thruster-hull interactions, thruster-nearby structure interactions and ventilation.

Scope of Work

- Review of literature on Underwater Snake Robots (USR)
- Study possible thrust losses and quantify these by simplified methods
- Carry out a simulation study of in-line velocity fluctuations and transverse velocity fluctuations
- Do full scale testing of the underwater snake robot with thrusters at Eelume and determine to what extent the thrust losses affect the robot
- Report the work

The report shall be written in English and edited as a research report including literature survey, description of mathematical models, description of control algorithms, simulation results, model test results, discussion and a conclusion including a proposal for further work. Source code should be provided on a CD, memory stick or similar. It is supposed that Eelume and the Department of Marine Technology, NTNU, can use the results freely in its research work, unless otherwise agreed upon, by referring to the student's work. The thesis should be submitted in two copies within August 26^{th}.

Co-supervisor: PostDoc Researcher Eleni Kelasidi

Supervisor: Prof. Asgeir J. Sørensen

Preface

This master thesis has been written spring/summer 2017 at Norwegian University of Science and Technology (NTNU), Department of Marine Technology. The master thesis is a continuation of the pre project thesis found in Galta (2017). Theory of the underwater snake robot is reviewed and the theory of the thrust losses is extended. Simulations are done in MATLAB and full scale testing of the robot is done at Eelume.

The software code used for the simulations in MATLAB, is developed by Eleni Kelasidi. The author of this thesis has updated the software code to account for thrust losses as well. Results from the simulations are given in the thesis.

Trondheim, 26^{th} of August

Mari Gilje Galta

Abstract

The main motivation behind this thesis is to study the effects from different thrust losses on an underwater snake robot (USR) with thrusters. In-line velocity fluctuations, transverse velocity fluctuations, thruster-thruster interactions, thruster-hull interactions, thurster-nearby structure interactions and ventilation are studied. First, an extensive literature study is done for the modeling of underwater snake robots with and without thrusters, propeller characteristics and thrust losses.

In-line and transverse velocity fluctuations are simulated in MATLAB. It is shown that the smaller the model is and the higher the shaft speed is, the bigger the thrust losses become. In-line velocity fluctuations are present as long as thrust is given from at least one of the thrusters, while transverse velocity fluctuations are present as long as there is a normal velocity component close to the thruster. The influence of the K_T-value (non-dimensional thrust coefficient) is also studied. A smaller K_T-value, gives a larger effect from the thrust losses. By adding current it is shown that the current changes the velocities in the x- and y-directions of the robot, which leads to the thrust losses increasing or decreasing in the respective directions.

Observations are done using the USR at Eelume to study the rest of the thrust losses. When the configuration is as given in this thesis, the effects from the thruster-thruster interactions, thruster-hull interactions and thurster-nearby structure interactions seem to be negligible. Ventilation is present when the USR is near the water surface.

Sammendrag

Hovedmotivasjonen bak denne oppgaven er å studere effekten av ulike trusttap på en undervanns slangerobot (USR) med trustere. Tangentielle hastighetsfluktuasjoner, normale hastighetsfluktuasjoner, truster-truster interaksjoner, truster-skrog interaksjoner, truster-nærliggende struktur interaksjoner og ventilasjon er studert. Det er først gjort et omfattende litteraturstudium om modellering av slangeroboter under vann med og uten trustere, propellkarakteristikk og trusttap.

Tangentielle og normale hastighetsfluktuasjoner er simulert i MATLAB. Her vies det at jo mindre modellen er og jo høyere fart som brukes, desto større blir trusttapene. Tangentielle hastighetsfluktuasjoner er tilstede så lenge det gis trust ut av minst en av trusterne, mens normale hastighetsfluktuasjoner er tilstede så lenge en normal hastighetskomponent er i nærheten av trusteren. Innflytelsen av K_T-verdien (dimensjonsløs trust koeffisient) er også studert. Desto mindre K_T-verdien er, jo større blir trusttapene. Ved å bruk av strøm i simuleringsmodellen, ser man at farten påvirkes i x- og y-retning, som fører til at trusttapene øker eller minker i den respektive retningen.

Fullskala tester av slangeroboten med trustere er gjort hos Eelume for å studere de resterende trusttapene. Ved å bruke konfigurasjonen som det er tatt utgangspunkt i i denne oppgaven, så ser man at effekten av truster-truster interaksjoner, truster-skrog interaksjoner og truster-nærliggende struktur interaksjoner ser ut til å være neglisjerbar. Ventilasjon er tilstede når slangeroboten er nær vannoverflaten.

Acknowledgments

I would like to thank professor Asgeir J. Sørensen for being my supervisor at NTNU, and for giving me motivation, feedback and guidance during this study. Our frequent meetings have helped me getting the insight I needed about propellers and thrust losses, and organization of this thesis. I would also like to thank both my supervisor and PhD candidate Jørgen Sverdrup-Thygeson for helping me with the full scale testing of the underwater snake robot at Eelume.

I would like to extend a gratitude to professor Kristin Ytterstad Pettersen for defining a problem description for my master thesis together with my supervisor. I would also like to thank CTO Pål Liljebäck and Henning Stenersen from Eelume for giving me the information I needed about the underwater snake robot's configuration and its thrusters. I especially want to thank my co-supervisor PostDoc researcher Eleni Kelasidi for giving me the software code used for my simulations, for following up on my progress and for giving me feedback.

Finally, I would like to thank my friends and family for their support and motivation during this progress.

Nomenclature

In general scalars are given by normal lowercase (a) or uppercase (A) letters, while vectors are given by boldface lowercase letters (**b**) and matrices are given by boldface uppercase letters (**B**).

(p_x, p_y) Global coordinates of the CM of the robot

(x_i, y_i) Global coordinates of the CM of link i

$\bar{\theta}$	Heading of the underwater snake robot	$[rad]$
β_{Q_a}	Torque loss factor for in-line velocity fluctuations	$[-]$
$\beta_{T,tr}$	Thrust loss factor for transverse velocity fluctuations	$[-]$
β_{T_a}	Thrust loss factor for in-line velocity fluctuations	$[-]$
$\boldsymbol{\mu}$	Matrix of the added mass	$[kg]$
$\boldsymbol{\phi}$	Vector of the different joint angles	$[rad]$
$\boldsymbol{\theta}$	Vector of the different global angles	$[rad]$
$\boldsymbol{b_x}$	x-component of the added effectors	$[-]$
$\boldsymbol{b_y}$	y-component of the added effectors	$[-]$
$\boldsymbol{f_{Dx}^{II}}$	Vector of the forces due to nonlinear drag in the x-direction	$[N]$
$\boldsymbol{f_{Dy}^{II}}$	Vector of the forces due to nonlinear drag in the y-direction	$[N]$
$\boldsymbol{f_{Dx}^{I}}$	Vector of the forces due to linear drag in the x-direction	$[N]$

$\boldsymbol{f_{Dy}^I}$	Vector of the forces due to linear drag in the y-direction	$[N]$
$\boldsymbol{f_{Ax}}$	Vector of the forces due to added mass in the x-direction	$[N]$
$\boldsymbol{f_{Ay}}$	Vector of the forces due to added mass in the y-direction	$[N]$
$\boldsymbol{f_{tx}}$	Vector of the forces from the added effectors in the x-direction	$[N]$
$\boldsymbol{f_{ty}}$	Vector of the forces from the added effectors in the y-direction	$[N]$
$\boldsymbol{f_t}$	Vector of the magnitudes of forces due to added effectors	$[N]$
$\boldsymbol{f_x}$	Vector of the fluid forces in the x-direction	$[N]$
$\boldsymbol{f_y}$	Vector of the fluid forces in the y-direction	$[N]$
$\boldsymbol{h_x}$	Vector of the joint constraint forces in the x-direction	$[N]$
$\boldsymbol{h_y}$	Vector of the joint constraint forces in the y-direction	$[N]$
$\boldsymbol{J}$	Matrix of the different link inertias	$[kgs^2]$
$\boldsymbol{K}_{tr}$	Thrust loss matrix	$[-]$
$\boldsymbol{L}$	Matrix of the different link half lengths	$[m]$
$\boldsymbol{M}$	Matrix of the different link masses	$[kg]$
$\boldsymbol{u_d}$	Control vector of propeller inputs	$[-]$
$\boldsymbol{V_{r_x}}$	Vector of the relative velocity in the x-direction	$[m/s]$
$\boldsymbol{V_{r_y}}$	Vector of the relative velocity in the y-direction	$[m/s]$
$\boldsymbol{V_x}$	Vector of the ocean current velocities in the x-direction	$[m/s]$
$\boldsymbol{V_y}$	Vector of the ocean current velocities in the y-direction	$[m/s]$
$\lambda_{1,i}$	Added mass parameter	$[kgm]$

$\lambda_{2,i}$, $\lambda_{3,i}$	Nonlinear and linear drag torque parameters	$[kgm]$
μ_i	Added mass	$[kg]$
ϕ	Angle between joint i and joint $i+1$	$[rad]$
ρ	Density of water	$[kg/m^3]$
τ	Control vector	$[-]$
τ_i	Fluid torque on the links	$[Nm]$
θ_i	Angle between i and the global x axis	$[rad]$
ζ_i	Direction of the added effector in the local frame	$[rad]$
C_A	Added mass coefficient	$[-]$
C_f, C_D	Drag coefficients	$[-]$
C_M	Added inertia coefficient	$[-]$
$c_{N,i}$	Drag parameter due to the two sides of the body in the normal direction	$[N/s]$
$c_{T,i}$	Drag parameter due to the two sides of the body in the tangential direction	$[N/s]$
e_{1i}, e_{2i}	Major and minor diameter of the cylindrical links	$[m]$
$f^{II}_{Dx,i}$	Force due to nonlinear drag in x-direction on link i	$[N]$
$f^{II}_{Dy,i}$	Force due to nonlinear drag in y-direction on link i	$[N]$
$f^{I}_{Dx,i}$	Force due to linear drag in x-direction on link i	$[N]$
$f^{I}_{Dy,i}$	Force due to linear drag in y-direction on link i	$[N]$
F_t	Force due to cross-coupling drag	$[N]$
$f_{Ax,i}$	Force due to added mass in x-direction on link i	$[N]$

$f_{Ay,i}$	Force due to added mass in y-direction on link i	$[N]$
$f_{t,i}$	Magnitude of forces due to added effectors	$[N]$
$f_{t,i}$	Magnitude of the force due to added effectors	$[N]$
$f_{tx,i}$	Force from the added effectors in the x-direction	$[N]$
$f_{ty,i}$	Force from the added effectors in the y-direction	$[N]$
$f_{x,i}$	Fluid force in x-direction on link i	$[N]$
$f_{y,i}$	Fluid force in y-direction on link i	$[N]$
$h_{x,i}$	Joint constraint force in the x-direction on link i from link $i+1$	$[N]$
$h_{y,i}$	Joint constraint force in the y-direction on link i from link $i+1$	$[N]$
J_a	Advance ratio	$[-]$
J_i	Moment of inertia of each link	$[kgs^2]$
K_Q	Torque coefficient	$[-]$
K_T	Thrust coefficient	$[-]$
K_{cc}	Cross-coupling drag factor	$[-]$
K_{Q0}	Nominal torque coefficient	$[-]$
K_{QC}	Control torque coefficient	$[-]$
K_{T0}	Nominal thrust coefficient	$[-]$
K_{TC}	Control thrust coefficient	$[-]$
l_i	Half the length of each link	$[m]$
m_i	The mass of each link	$[kg]$

m_t	Total mass	$[kg]$
N	Number of links	
n	The shaft speed	$[rad/s]$
P_a	Actual power	$[J/s]$
P_n	Nominal power	$[J/s]$
P_r	Reference power	$[Nm]$
Q_a	Actual torque	$[Nm]$
Q_n	Nominal torque	$[Nm]$
Q_{cn}	Commanded torque	$[Nm]$
Q_r	Reference torque	$[Nm]$
r	Total number of additional effectors	$[-]$
s	Degrees of freedom	$[-]$
T	Time constant	$[s]$
T_a	Actual thrust	$[N]$
T_d	Desired thrust	$[N]$
T_d	Thrust from the produced thrusters	$[-]$
T_n	Nominal thrust	$[N]$
U	Ship speed	$[m/s]$
V_a	Inflow velocity to the propeller	$[m/s]$
$V_{r_{x,i}}$	Relative velocity in the x-direction	$[m/s]$
$V_{r_{y,i}}$	Relative velocity in the y-direction	$[m/s]$

V_{tr}	Transverse velocity component	$[m/s]$
$V_{x,i}$	Ocean current velocities in the x-direction	$[m/s]$
$V_{y,i}$	Ocean current velocities in the y-direction	$[m/s]$
w	Wake fraction number	$[-]$
w_p	Wake fraction caused by so called potential effects for a hull advancing forward in an ideal fluid	$[-]$
w_v	Wake fraction caused by viscous effects due to the effect of boundary layers	$[-]$
w_w	Wake fraction caused by the wave motion of the water particles	$[-]$

Acronyms

AUV	Autonomous Underwater Vehicle
CM	Center of Mass
DOF	Degrees of Freedom
IMR	Inspection, Maintenance and Repair
ROV	Remotely Operated Vehicle
USM	Underwater Swimming Manipulator
USR	Underwater Swimming Robot
UUV	Unmanned Underwater Vehicles
UVMS	Underwater Vehicle Manipulator Systems

Physical Constants

Cross-coupling drag factor	K_{cc}	$=$	0.25 $[-]$
Density of freshwater	ρ	$=$	1000 $[kg/m^3]$
Gravity	g	$=$	9.81 $[m/s^2]$

Contents

Preface i

Abstract ii

Sammendrag iv

Acknowledgments vi

Nomenclature ix

List of Figures xix

List of Tables xxi

1 Introduction 1

1.1 Motivation 1

1.2 Objective and Limitations 3

1.3 Previous Work 4

1.3.1 Snake Robotics 4

1.3.2 Propulsion 5

1.4 Main Contributions 5

1.5 Organization of the Thesis 6

2 Literature Overview of Snake Robotics 7

2.1 Snake Locomotion 8

2.2 Biomimic Developed Concepts 11
2.2.1 ACM III 11
2.2.2 Anna Konda 12
2.2.3 Wheeko 12
2.2.4 Kulko 13
2.2.5 Mamba 13
2.3 Underwater Snake Robot with Thrusters 14

3 USR with Added Effectors 17
3.1 Kinematics of Underwater Snake Robot 19
3.2 Hydrodynamic Modeling 20
3.3 Forces from Added Effectors 23
3.4 Equations of Motion 23

4 Propellers and Thrusters 27
4.1 Propeller Characteristics 27
4.2 BlueRobotics T200 Thrusters 30
4.3 Thruster Dynamics 31
4.4 Thrust Losses 32
4.4.1 In-Line Velocity Fluctuations 32
4.4.2 Transverse Velocity Fluctuations 33
4.4.3 Thruster-Thruster Interactions 34
4.4.4 Thruster-Hull Interactions 35
4.4.5 Thruster-Nearby Structure Interactions 36
4.4.6 Ventilation 36
4.5 Thruster Control 37
4.5.1 Thruster Allocation 37
4.5.2 Truster Controllers 39

5 Simulations 41
5.1 Simulations in MATLAB 42

5.1.1 Comparing Nominal Thrust, In-Line Velocity Fluctuations, and In-Line and Transverse Velocity Fluctuations . . . 43
5.1.2 The Influence of K_T . . . 60
5.1.3 Adding Current . . . 65
5.2 Full Scale Testing of Underwater Snake Robot . . . 70
5.2.1 Thruster-Thruster Interactions . . . 70
5.2.2 Thruster-Hull Interactions . . . 71
5.2.3 Thruster-Nearby Structure Interactions . . . 72
5.2.4 Ventilation . . . 72
5.3 Discussion . . . 72
5.3.1 Simulations in MATLAB . . . 72
5.3.2 Full Scale Testing . . . 79
5.3.3 Control System . . . 80

6 Concluding Remarks **83**
6.1 Conclusions . . . 83
6.2 Further Work . . . 84

Bibliography **86**

A Basic Notation **A**

B Input Data **E**
B.1 In-Line Velocity Fluctuations . . . G
B.2 Transverse Velocity Fluctuations . . . H

C MATLAB Code **I**

List of Figures

1.1 Examples of typical ROV and AUV 2
1.2 Model of the underwater swimming robot with thrusters. Given in Maritime (2017) 4

2.1 Potential applications for snake robots 8
2.2 Biological snake locomotion from Liljebäck et al. (2012a) 9
2.3 The snake robot ACM III, which was the world's first snake robot developed by professor Shigeo Hirose in 1972. From Hirose and Yamada (2009) 11
2.4 The fire fighting snake robot Anna Konda. Found in ROBOTNOR (2017a) 12
2.5 The snake robot Wheeko from Liljebäck et al. (2012a) . 13
2.6 The snake robot Kulko, found in Liljebäck et al. (2012b) 13
2.7 The amphibious snake robot Mamba 14
2.8 Model of the underwater swimming robot with thrusters. Found in Eelume (2017) 15

3.1 Kinematic parameters of the USR moving in the horizontal plane found in Kelasidi (2015). In this figure, n is the number of links 18
3.2 Forces and torques acting on each link of the USR moving in the horizontal plane taken from Kelasidi (2015) . 18

4.1 Example of open water characeristics found in Sørensen (2013). K_T is given by a solid line and $10 \cdot K_Q$ by a dashed line 29
4.2 T2 Thrusters from BlueRobotics 31
4.3 The parameter p_0 is the pressure far away, V is the robot's velocity, p_1 is the pressure right in front of the propeller, p_2 is the pressure right behind the propeller, V_p is the velocity at the propeller and U_A is the induced velocity given by the wake. Found in Steen (2014) . . . 34
4.4 The Coanda effect from Faltinsen (1990). 35
4.5 A control system of the underwater snake robot 38

5.1 Tests done with low speed for case 1 45
5.2 Tests done with high speed for case 1 47
5.3 Tests done with low speed for case 2 49
5.4 Tests done with high speed for case 2 51
5.5 Tests done with low speed for case 3 54
5.6 Tests done with high speed for case 3 56
5.7 Tests done with low speed for case 4 58
5.8 Tests done with high speed for case 4 60
5.9 Tests done to test the influence of K_T in low speeds . . 63
5.10 Tests done to test the influence of K_T in high speeds . 65
5.11 Tests done to study the performance of the underwater snake robot with low speeds in current 67
5.12 Tests done to study the performance of the underwater snake robot with high speeds in current 69
5.13 Pool with underwater snake robot at Eelume 70
5.14 The configuration of the underwater snake robot with thrusters used in full scale testing at Eelume 71

B.1 The model of the Underwater Snake Robot with thrusters used in MATLAB . . . . . F

B.2 Propeller open water characteristics used in the simulations in this thesis . . . . . G

List of Tables

4.1 Performance of the T200 Thrusters 31

5.1 Dimensions of the small and the actual model 43
5.2 Shaft speed and angle of attack for each thruster on the underwater snake robot when testing low speeds in case 1 44
5.3 Shaft speed and angle of attack for each thruster on the underwater snake robot when testing high speeds in case 1 46
5.4 Shaft speed and angle of attack for each thruster on the underwater snake robot when testing low speeds in case 2 48
5.5 Shaft speed and angle of attack for each thruster on the underwater snake robot when testing high speeds in case 2 50
5.6 Shaft speed and angle of attack for each thruster on the underwater snake robot when testing low speeds in case 3 52
5.7 Shaft speed and angle of attack for each thruster on the underwater snake robot when testing high speeds in case 3 54
5.8 Shaft speed and angle of attack for each thruster on the underwater snake robot when testing low speeds in case 4 57
5.9 Shaft speed and angle of attack for each thruster on the underwater snake robot when testing high speeds in case 4 59

5.10 Different K_T-values for each J_a-value 60
5.11 Shaft speed and angle of attack for each thruster when testing K_T-values with low speed 61
5.12 Shaft speed and angle of attack for each thruster when testing K_T-values with high speed 63
5.13 Shaft speed and angle of attack for each thruster when testing the underwater snake robot on low speeds in current 66
5.14 Shaft speed and angle of attack for each thruster when testing the underwater snake robot on high speeds in current 68

Chapter 1

Introduction

This section gives an introduction to the thesis with some motivational aspects and references to previous work. An overview of the report is also presented.

1.1 Motivation

The focus on subsea installations and operations in the oil and gas industry has been increasing the last decade. The need for installation support and subsea inspection, maintenance and repair (IMR) are therefore also increasing. Unmanned Underwater Vehicles (UUVs) are usually used for inspection and intervention of subsea structures. There are mainly two types of UUVs; Remotely Operated Vehicles (ROV) and Autonomous Underwater Vehicles (AUV). An example of a ROV is shown in figure 1.1a. ROVs are often used for installation, maintenance and inspection of subsea installations. They are linked to a host ship by a neutrally buoyant tether and are often equipped with cameras and manipulator arm(s), also called Underwater Vehicle Manipulator Systems (UVMSs). ROVs are in general large, heavy, expensive to operate, require constant supervision and the time needed to mobilize and deploy them is quite long. The need for a vehicle that

was less costly, smaller and lightweighted lead to the development of the AUV. AUVs can perform routine inspection tasks at subsea oil and gas installations and has hovering capabilities. A typical AUV is shown in figure 1.1b. AUVs are autonomous and often pre-programmed to follow a desired path. They are often used for mapping and inspection of the seabed.

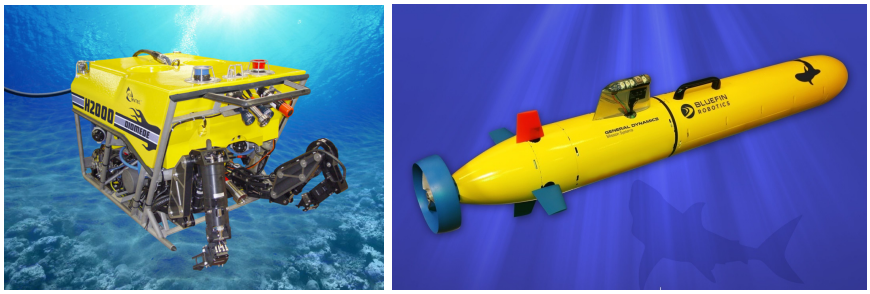

(a) An example of a typical ROV (ROBO-NEWS, 2017)

(b) An example of a typical AUV (Technology, 2017)

Figure 1.1: Examples of typical ROV and AUV

Using nature as an inspiration, efficiency and maneuverability can be improved further. A robot moving like a snake can move in challenging environments and has the ability to transverse irregular environments. Eelume is a spin-off company from NTNU who got inspired by this and develops robotic snakes today. Underwater Snake Robots (USRs) are robots inspired by the biological swimming snakes and eels.

An USR is a robot with several links connected by joints which gives it the opportunity to move as a snake. The USR uses its own locomotion to move forward. An Underwater Swimming Manipulator (USM) is a cross-over between a typical ROV/AUV and an USR. The USM is an USR equipped with additional effectors. These effectors can be thrusters, propellers, fins, arms and/or other equipment. The effectors can be used to help the snake robot with better maneuver-

ability, proving to the robot hovering capabilities or they can help the robot serve as a manipulator.

When the underwater snake robot is equipped with thrusters, it is important to understand how thrusters work and act in water. Because of current, waves, interactions with other structures and interactions with its own thrusters and hull, thrust losses will occur. Thrust losses on ships are studied in detail, while there is a lot of uncertainties concerning thrust losses on underwater vehicles.

This thesis will study which kinds of thrust losses that will have a big impact on the underwater snake robot. The underwater snake robot will usually be deeply submerged, hence this will be focused on in the thesis in addition to a quick preview of ventilation.

1.2 Objective and Limitations

This thesis will study underwater snake robots with N links connected by *N-1* joints with main propellers and tunnel thrusters along the body. An example of an underwater snake robot with thrusters studied in this thesis is shown in figure 1.2. Both the main propellers and the tunnel thrusters are T200 Thrusters by BlueRobotics and are shown in figure 4.2. Possible thrust losses will be studied and quantified by simplified methods. Some of the thrust losses will be simulated in MATLAB, while the other losses will be studied by a preliminary full scale testing of the underwater snake robot at Eelume.

Some limitations have been made to simplify this task:

- The underwater snake robot is assumed to operate in the 2D virtual horizontal plane.
- The underwater snake robot is assumed to use positive shaft speeds.
- The underwater snake robot is deeply submerged, i.e. there are

Figure 1.2: Model of the underwater swimming robot with thrusters. Given in Maritime (2017)

no waves effecting the body.

- The links of the underwater snake robot are assumed to be neutrally buoyant. Thus links with thrusters have the exact same mass as the links with no thrusters.
- The sum of all torques on the links are assumed to be equal to zero.

1.3 Previous Work

It is naturally to divide the thesis into to main topics: one part about underwater snake robotics and one part about the propulsion. The previous work done in both of these areas are mentioned below.

1.3.1 Snake Robotics

Liljebäck et al. (2012a) and Transeth (2007) are used for understanding the movements of the snake and to get the mathematical models of a snake robot on the ground. Using Liljebäck et al. (2012a) as a reference, Kelasidi (2015), Kelasidi et al. (2014a), Kelasidi et al. (2014b),

Kelasidi et al. (2014c) and Kelasidi et al. (2015) derive the hydrodynamic effects and the equations of motion for an underwater snake robot. The equations for an USR with added effectors are derived in Sverdrup-Thygeson et al. (2016a), Sverdrup-Thygeson et al. (2016b) and Kelasidi et al. (2017), and are used for the underwater snake robot with thrusters in this thesis.

1.3.2 Propulsion

For propulsion control and thruster allocation, work by Smogeli (2006), Ruth (2008) and Sørensen (2013) is used through the thesis. During study of propeller characteristics, Smogeli (2006) is mainly used, while Sørensen (2013) is mainly used when studying the thruster dynamics.

An extensive study of different thrust losses is given in Lehn (1992), Faltinsen (1990), Steen (2014) and Faltinsen (2005).

1.4 Main Contributions

The main contributions in this thesis is the study of thrust losses on underwater snake robots. In-line and transverse velocity fluctuations are simulated using MATLAB. To calculate the effects of these losses, an open water characteristics for the 1^{st} quadrant is assumed.

Other losses, like thruster-thruster interactions, thruster-hull interactions, thruster-nearby structure interactions and ventilation, are studied by doing preliminary full scale testing of the underwater snake robot at Eelume where the importance of each thrust loss is determined.

1.5 Organization of the Thesis

The report is organized as follows.

Chapter 2 represents a review of snake locomotion. Some biomimic developed concepts are mentioned and the underwater snake robot with thrusters are introduced.

Chapter 3 gives a general introduction to the modeling of the underwater snake robot with added effectors.

Chapter 4 presents the thrusters used on the model. In this chapter the propeller characteristics and thruster dynamics are also discussed. Possible thrust losses, the thruster allocation algorithm and different thruster controllers are described.

Chapter 5 includes a simulation study of in-line velocity fluctuations and transverse velocity fluctuations. A full scale test is done at Eelume to study thruster-thruster interactions, thruster-hull interactions, thruster-nearby structure interactions and ventilation. The discussion of the results of the simulations and the full scale testing is in the end of this chapter.

Chapter 6 gives the conclusion of the thesis and proposals for further work.

Chapter 2

Short Literature Overview of Snake Robotics

The biological snake has several properties that is outstanding for this precise animal. Their small cross sections compared to their length allows them to maneuver through confined areas such as inside of pipes or other tight structures. The ability to change their body shape gives them the possibility to perform a wide range of behaviors, such as sliding forward, climbing and swimming.

A snake robot is a biomorphic hyper-redundant robot that resembles a biological snake. The idea behind snake robots is to construct robots that can have similar properties as snakes. Snake robots are useful in situations where their unique characteristics give them an advantage over the environment. The robots will be able to do things that would be difficult for humans, such as searching collapsed homes after earthquakes and carrying out checks on infrastructure. Some potential applications, such as rescue and fire-fighting, pipeline maintenance and underwater manipulation are shown in figure 2.1.

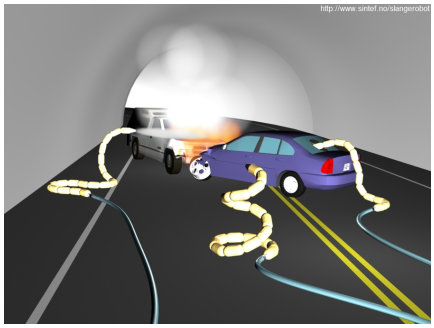

(a) Fire figting snake robot from SINTEF (2017b)

(b) Pipeline maintanance from Robotics and Systems (2017)

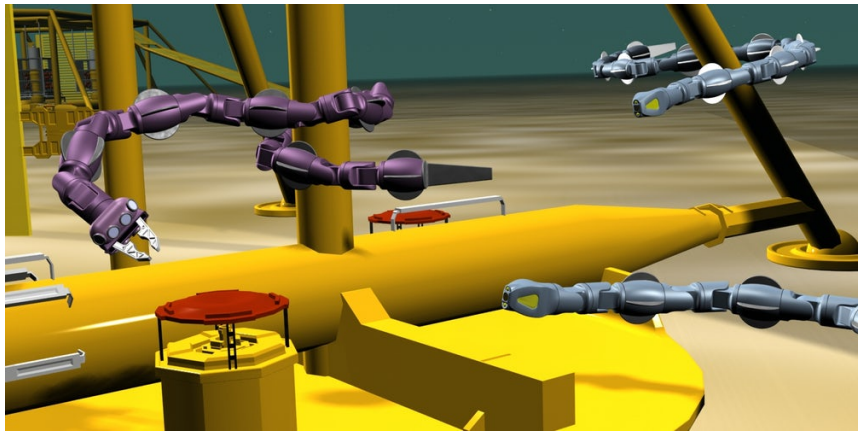

(c) Underwater manipulation from Trendhunter (2017)

Figure 2.1: Potential applications for snake robots

In the following sections, different snake locomotion will be represented and a short review of some of the snake robots made so far is given. In the end, the underwater snake robot which is used in this thesis will be represented.

2.1 Snake Locomotion

Instead of using legs, the snake robot uses its own body to move forward. This is called snake-like locomotion. The most common types of biological snake locomotion are lateral undulation, concertina loco-

motion, rectilinear crawling and sidewinding as explained in (Liljebäck et al., 2012a). These are shown in figure 2.2.

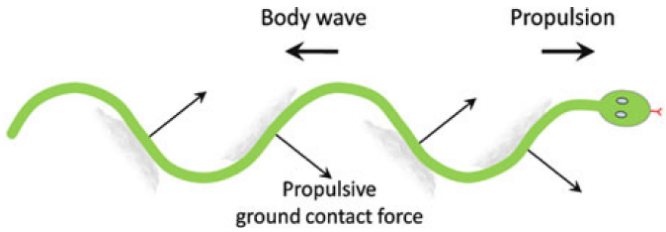

(a) Lateral undulation.

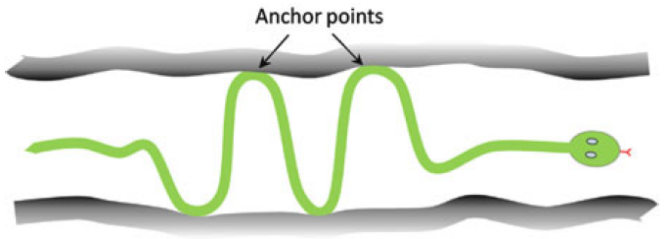

(b) Concertina undulation

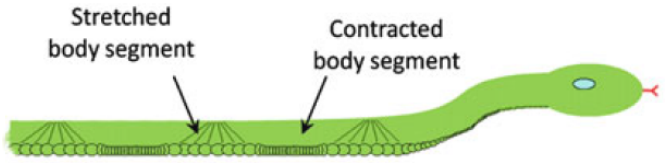

(c) Rectilinear undulation

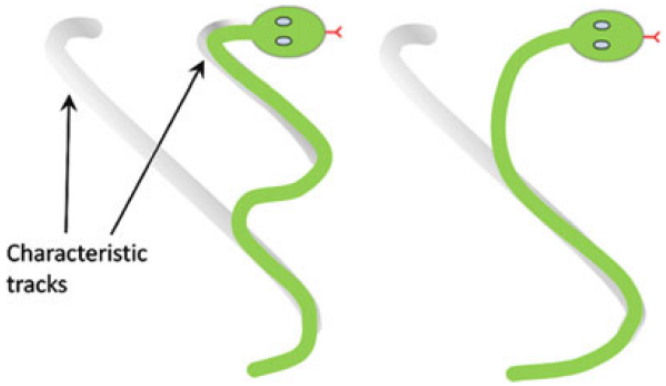

(d) Sidewinding

Figure 2.2: Biological snake locomotion from Liljebäck et al. (2012a)

Lateral undulation, shown in figure 2.2a, is the fastest and most common form of snake locomotion. This locomotion is achieved by creating continuous body waves with constant amplitude which are propagated backwards from head to tail as described in Liljebäck et al. (2012a) and Kelasidi (2015). While moving like this, the sides of the snake body pushes against the resistance of the water, thereby pushing the snake forward.

Concertina locomotion is a motion which is most useful in narrow spaces. The locomotion is achieved by stretching the front part of the body forward while the back part of the body is curved several times. This leads to an anchor against the narrow environment as shown in figure 2.2b. When the front part is fully extended, it is used to create an anchor for the back part using the same method.

Rectilinear crawling is usually used on heavy snakes. The snake moves in approximately a straight line using the edges of the scales on its underside as anchor points. It stretches forward, hooks the edges of the scales over small irregularities and pulls the body to this point. Different parts of the body will stretch and pull at the same time. This is shown in figure 2.2c.

Sidewinding is shown in figure 2.2d. This motion is created by using one part of the body as an anchor, while the rest of the body raises its part up and throws it sideways. The movement starts in resting position, then the front part lifts itself up and is thrown sideways while the rest of the body behave as an anchor. After this, the rest of the body lifts itself up in turn while the front acts as the anchor.

2.2 Biomimic Developed Concepts

Biomimetic means that humans get inspiration from the nature to create systems or devices. Hence how the snake robots have some of the characteristics as biological snakes. In the following some of the biomimic concepts that have been developed will be represented.

2.2.1 ACM III

ACM III is developed by professor Shigeo Hirose at Tokyo Institute of Technology in 1972 and is shown in figure 2.3. The robot is equipped with wheels along its body which make it possible for the robot to move forward on a flat surface. By controlling the joints, a serpentine motion can be achieved by using the same locomotion principle as a real snake. According to Hirose and Yamada (2009), this is the first robot in the world that can move as a snake.

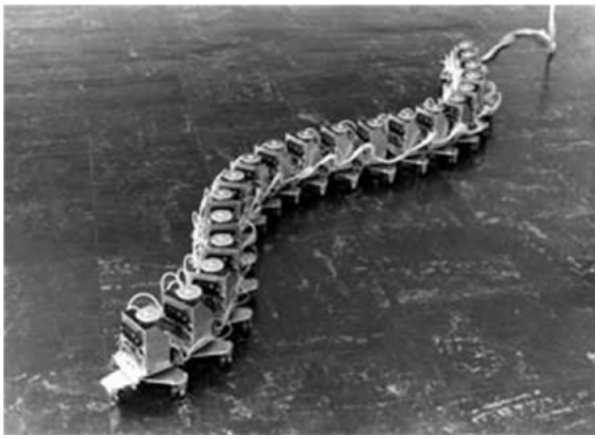

Figure 2.3: The snake robot ACM III, which was the world's first snake robot developed by professor Shigeo Hirose in 1972. From Hirose and Yamada (2009)

2.2.2 Anna Konda

Anna Konda is a fire fighting snake robot developed by SINTEF and is shown in figure 2.4. It works as a self-propelled fire hose that can climb into buildings and extinguish a fire. This way no human fire fighters will be at risk. As explained in SINTEF (2017a) and ROBOTNOR (2017a), the snake moves like a biological snake by equipping the fire house with water hydraulic actuators. The water in the fire hose have the following functions: it extinguish the fire with water, the robot gets cooled down by the water and hydraulic actuation by moving the joints of the robot with pressurized water. Anna Konda moves like a biological snake and can also raise its head to spray water.

Figure 2.4: The fire fighting snake robot Anna Konda. Found in ROBOTNOR (2017a)

2.2.3 Wheeko

Wheeko is a snake robot with passive wheels, shown in figure 2.5. The snake robot is developed to do experiments related to snake robot locomotion across flat surfaces. According to ROBOTNOR (2017d) and Liljebäck et al. (2012a), each of the ten joint modules have two motorized degrees of freedom and are covered by passive wheels. These wheels make it possible to move forward over a flat surface.

Figure 2.5: The snake robot Wheeko from Liljebäck et al. (2012a)

2.2.4 Kulko

Kulko, seen in figure 2.6, is a snake robot developed to help with investigation of locomotion in uneven and cluttered environments as explained in ROBOTNOR (2017b), Liljebäck et al. (2012a) and Liljebäck et al. (2010). By having a smooth exterior surface, the robot can achieve a gliding motion in a cluttered environment. A contact force sensing system is added to sense the environment and use the irregularities as pushpoints to aid the propulsion.

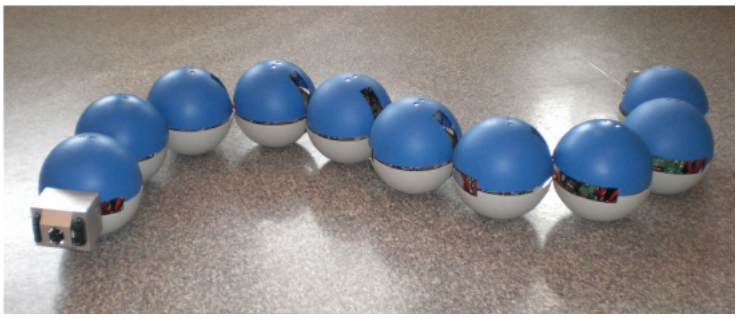

Figure 2.6: The snake robot Kulko, found in Liljebäck et al. (2012b)

2.2.5 Mamba

Mamba is an amphibious snake robot which can move on the ground and in water as shown in figure 2.7. The robot is used to research the

snake locomotion on the ground and in water. According to ROBOTNOR (2017c) and Liljebäck et al. (2014), the underwater snake robot has the ability to measure environment contact forces acting along its body. Thus this sensor system allows demonstration of adaptive snake robot locomotion in outdoor environments.

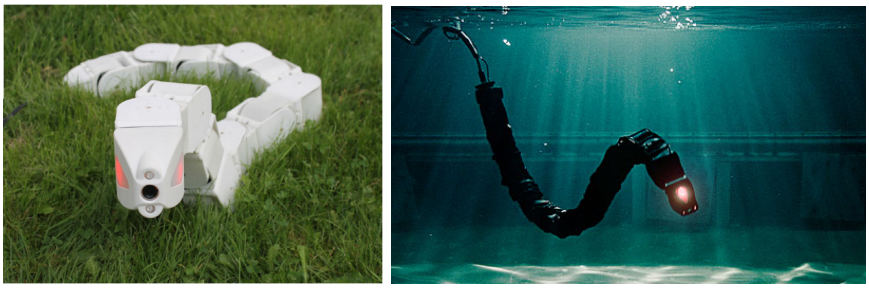

(a) Moving on the ground. Found in Liljebäck et al. (2014)

(b) Swimming in water. Found in Nysgjerrigper (2017)

Figure 2.7: The amphibious snake robot Mamba

2.3 Underwater Snake Robot with Thrusters

All of the snake robots mentioned above are developed for different purposes. The underwater snake robot with thrusters studied in this thesis, has the purpose of inspection and maintenance of subsea installations. Hence cameras are added to the robot and there is a possibility to mount different equipment on the front link. While inspecting the subsea installation, the underwater snake robot needs to be in station keeping. Thus thrusters are needed. By adding thrusters, the maneuverability, flexibility and hovering capabilities are improved. Figure 2.8 represents the model of the underwater snake robot with thrusters.

Figure 2.8: Model of the underwater swimming robot with thrusters. Found in Eelume (2017)

Chapter 3

USR with Added Effectors

The underwater snake robot studied in this thesis is an underwater snake robot with thrusters. Because of the thrusters, the underwater snake robot is acting like a manipulator. The robot consists of N rigid links which are interconnected by $N-1$ joints. The links are numbered from $i = 1$ to $i = N$ from tail to head. Each link has a length of $2l_i$, mass m_i and moment of inertia $J_i = \frac{1}{3}m_i l_i^2$. The mass of each link is uniformly distributed, thus the center of mass (CM) is located at the midpoint. The sum of the mass of all of the links is given as the total mass, $m_t = \Sigma_{i=1}^{N} m_i$.

In the following sections, the kinematics, dynamics, hydrodynamic model and the equations of motion for the underwater snake robot moving in the virtual horizontal plane will be represented. The vectors and matrices shown in Appendix A are used in the following sections. Figure 3.1 shows the kinematics of the underwater snake robot, while the forces and torques acting on each link are shown in figure 3.2.

This chapter is mainly based on Kelasidi et al. (2017), and uses the same notations.

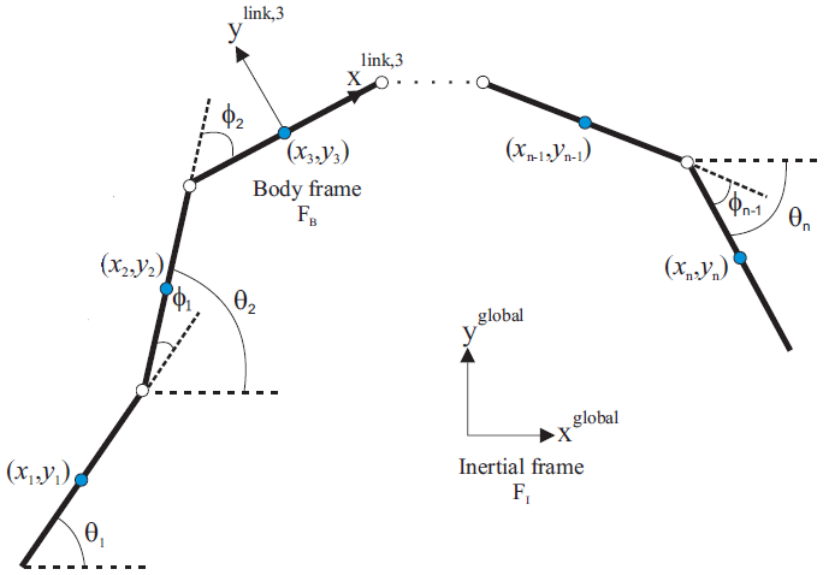

Figure 3.1: Kinematic parameters of the USR moving in the horizontal plane found in Kelasidi (2015). In this figure, n is the number of links

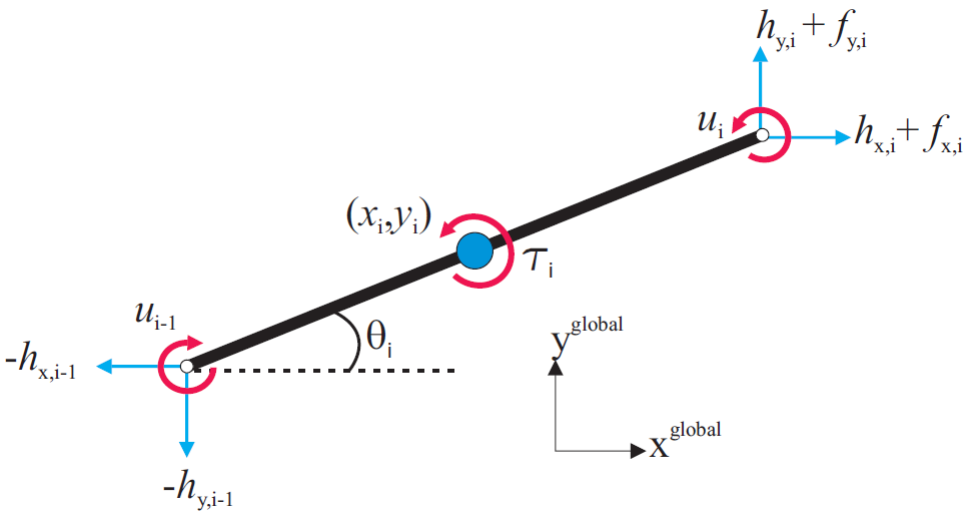

Figure 3.2: Forces and torques acting on each link of the USR moving in the horizontal plane taken from Kelasidi (2015)

3.1 Kinematics of Underwater Snake Robot

The underwater snake robot has $N + 2$ degrees of freedom (N link angles and the planar position of the center of mass of the robot). The *link angle* of each link $i \in \{1, ..., N\}$ of the robot, denoted as $\theta_i \in \mathbb{R}$, describes the orientation of a link with respect to the global x-axis, while the *joint angle* of joint $i \in \{1, ..., N-1\}$ is the difference between the link angles of two neighboring links, and is given by $\phi_i = \theta_i - \theta_{i+1}$. θ_i and ϕ_i are grouped in vectors $\boldsymbol{\theta} = [\theta_1, ...\theta_N]^T \in \mathbb{R}^N$ and $\boldsymbol{\phi} = [\phi_1, ..., \phi_{N-1}]^T \in \mathbb{R}^{N-1}$, respectively.

The *heading* of the underwater snake robot is denoted as $\bar{\theta} \in \mathbb{R}$ and is described as the average of all of the link angles:

$$\bar{\theta} = \frac{1}{N} \Sigma_{i=1}^{N} \theta_i. \tag{3.1}$$

The local coordinate system of each link of the underwater snake robot is centered in the CM of the link with the x-axis positioned alongside the tangential axis of the robot, while the y-axis is positioned normal to the link. When all the link angles are zero, the local coordinate axis will be aligned with the global coordinate axis. The rotation matrix from the global frame to the frame of each link i is given as

$$\boldsymbol{R}_{link,i}^{global} = \begin{bmatrix} cos(\theta_i) & -sin(\theta_i) \\ sin(\theta_i) & cos(\theta_i) \end{bmatrix}. \tag{3.2}$$

The global frame position $\boldsymbol{p}_{CM}$ of the CM of the robot is given by

$$\boldsymbol{p_{CM}} = \begin{bmatrix} p_x \\ p_y \end{bmatrix} = \begin{bmatrix} \frac{1}{m_t} \Sigma_{i=1}^{N} m_i x_i \\ \frac{1}{m_t} \Sigma_{i=1}^{N} m_i y_i \end{bmatrix} = \frac{1}{m_t} \begin{bmatrix} \boldsymbol{e}^T \boldsymbol{M} \boldsymbol{X} \\ \boldsymbol{e}^T \boldsymbol{M} \boldsymbol{Y} \end{bmatrix} \tag{3.3}$$

where $\boldsymbol{X} = [x_1, ..., x_N]^T \in \mathbb{R}^N$ and $\boldsymbol{Y} = [y_1, ..., y_N]^T \in \mathbb{R}^N$. The vector $\mathbf{e}$ and matrix $\mathbf{M}$ can be found in Appendix A.

The connection between link i and link $i+1$ at joint $i \in \{1, ..., N-1\}$ must comply with the two *holonomic* constraints:

$$\boldsymbol{DX} + \boldsymbol{AL}cos(\boldsymbol{\theta}) = \mathbf{0}, \qquad \boldsymbol{DY} + \boldsymbol{AL}sin(\boldsymbol{\theta}) = \mathbf{0} \tag{3.4}$$

where **D**, **A** and **L** are found in Appendix A.

By combining (3.3) and (3.4), the position of the individual links as a function of the CM position and the link angles of the robot are found:

$$\boldsymbol{X} = -\boldsymbol{K}^T cos\theta + \boldsymbol{e}p_x, \qquad \boldsymbol{Y} = -\boldsymbol{K}^T sin\theta + \boldsymbol{e}p_y \tag{3.5}$$

where **K** is found in Appendix A.

The linear velocities are found by differentiating (3.5) with respect to time, and are given by

$$\dot{\boldsymbol{X}} = \boldsymbol{K}^T \boldsymbol{S_\theta} \dot{\boldsymbol{\theta}} + \boldsymbol{e}\dot{p}_x, \qquad \dot{\boldsymbol{Y}} = -\boldsymbol{K}^T \boldsymbol{C_\theta} \dot{\boldsymbol{\theta}} + \boldsymbol{e}\dot{p}_y \tag{3.6}$$

where $\boldsymbol{S_\theta}$ and $\boldsymbol{C_\theta}$ are given in Appendix A.

By differentiating (3.6), the accelerations are found as

$$\ddot{\boldsymbol{X}} = \boldsymbol{K}^T(\boldsymbol{C_\theta}\dot{\boldsymbol{\theta}}^2 + \boldsymbol{S_\theta}\ddot{\boldsymbol{\theta}}) + \boldsymbol{e}\ddot{p}_x, \quad \ddot{\boldsymbol{Y}} = \boldsymbol{K}^T(\boldsymbol{S_\theta}\dot{\boldsymbol{\theta}}^2 - \boldsymbol{C_\theta}\ddot{\boldsymbol{\theta}}) + \boldsymbol{e}\ddot{p}_y \tag{3.7}$$

where $\dot{\boldsymbol{\theta}}^{\mathbf{2}}$ is found in Appendix A.

3.2 Hydrodynamic Modeling

As shown in Kelasidi et al. (2014b), Sverdrup-Thygeson et al. (2016b) and Kelasidi et al. (2017), the fluid forces on all links can be expressed as

$$\boldsymbol{f} = \begin{bmatrix} \boldsymbol{f_x} \\ \boldsymbol{f_y} \end{bmatrix} = \begin{bmatrix} \boldsymbol{f_{Ax}} \\ \boldsymbol{f_{Ay}} \end{bmatrix} + \begin{bmatrix} \boldsymbol{f^I_{D_x}} \\ \boldsymbol{f^I_{D_y}} \end{bmatrix} + \begin{bmatrix} \boldsymbol{f^{II}_{D_x}} \\ \boldsymbol{f^{II}_{D_y}} \end{bmatrix} \tag{3.8}$$

where $\boldsymbol{f_{D_x}^I}$ and $\boldsymbol{f_{D_y}^I}$ represent the effect from the linear drag forces, while $\boldsymbol{f_{D_x}^{II}}$ and $\boldsymbol{f_{D_y}^{II}}$ represent the effect from the nonlinear drag forces. The vectors $\boldsymbol{f_{A_x}}$ and $\boldsymbol{f_{A_y}}$ represent the effect from the added mass in the x- and y-direction. The linear and nonlinear drag forces are given by (3.9) and (3.10), respectively.

$$\begin{bmatrix} \boldsymbol{f_{D_x}^I} \\ \boldsymbol{f_{D_y}^I} \end{bmatrix} = - \begin{bmatrix} \boldsymbol{c_T C_\theta} & \boldsymbol{-c_N S_\theta} \\ \boldsymbol{c_T S_\theta} & \boldsymbol{c_N C_\theta} \end{bmatrix} \begin{bmatrix} \boldsymbol{V_{r_x}} \\ \boldsymbol{V_{r_y}} \end{bmatrix} \tag{3.9}$$

$$\begin{bmatrix} \boldsymbol{f_{D_x}^{II}} \\ \boldsymbol{f_{D_y}^{II}} \end{bmatrix} = - \begin{bmatrix} \boldsymbol{c_T C_\theta} & \boldsymbol{-c_N S_\theta} \\ \boldsymbol{c_T S_\theta} & \boldsymbol{c_N C_\theta} \end{bmatrix} sgn\left(\begin{bmatrix} \boldsymbol{V_{r_x}} \\ \boldsymbol{V_{r_y}} \end{bmatrix} \right) \begin{bmatrix} \boldsymbol{V_{r_x}}^2 \\ \boldsymbol{V_{r_y}}^2 \end{bmatrix} \tag{3.10}$$

where $\boldsymbol{c_T} = diag(c_{T,1}, ..., c_{T,N}) \in \mathbb{R}^{N \times N}$ and $\boldsymbol{c_N} = diag(c_{N,1}, ..., c_{N,N}) \in \mathbb{R}^{N \times N}$ represent the drag parameters due to the two sides of the body in the tangent and normal direction of each link. $\boldsymbol{V_{r_x}}$ and $\boldsymbol{V_{r_y}}$ are the relative velocities in the body frame and are given by

$$\begin{bmatrix} \boldsymbol{V_{r_x}} \\ \boldsymbol{V_{r_y}} \end{bmatrix} = \begin{bmatrix} \boldsymbol{C_\theta} & \boldsymbol{S_\theta} \\ \boldsymbol{-S_\theta} & \boldsymbol{C_\theta} \end{bmatrix} \begin{bmatrix} \boldsymbol{\dot{X}} - \boldsymbol{V}_x \\ \boldsymbol{\dot{Y}} - \boldsymbol{V}_y \end{bmatrix} \tag{3.11}$$

The vectors $\boldsymbol{V}_{(\cdot)}^2 = [V_{(\cdot)1}^2, ..., V_{(\cdot)N}^2] \in \mathbb{R}^N$, $\boldsymbol{V}_x = [V_{x,1}, ..., V_{x,N}] \in \mathbb{R}^N$ and $\boldsymbol{V}_y = [V_{y,1}, ..., V_{y,N}] \in \mathbb{R}^N$ are the ocean current velocities.

By differentiating (3.11), the relative accelerations of the links in the body frame are found:

$$\begin{bmatrix} \boldsymbol{\dot{V}_{r_x}} \\ \boldsymbol{\dot{V}_{r_y}} \end{bmatrix} = \begin{bmatrix} \boldsymbol{C_\theta} & \boldsymbol{S_\theta} \\ \boldsymbol{S_\theta} & \boldsymbol{C_\theta} \end{bmatrix} \begin{bmatrix} \boldsymbol{\ddot{X}} \\ \boldsymbol{\ddot{Y}} \end{bmatrix} + \begin{bmatrix} \boldsymbol{-S_\theta} & \boldsymbol{C_\theta} \\ \boldsymbol{-C_\theta} & \boldsymbol{-S_\theta} \end{bmatrix} \begin{bmatrix} diag(\boldsymbol{\dot{\theta}}) & \boldsymbol{0} \\ \boldsymbol{0} & diag(\boldsymbol{\dot{\theta}}) \end{bmatrix} \begin{bmatrix} \boldsymbol{\dot{X}} - \boldsymbol{V}_x \\ \boldsymbol{\dot{Y}} - \boldsymbol{V}_y \end{bmatrix} \tag{3.12}$$

Using he procedure from Kelasidi (2015), Kelasidi et al. (2014b) and Sverdrup-Thygeson et al. (2016b), the effects from the added mass are found and presented as

$$\begin{bmatrix} \boldsymbol{f_{A_x}} \\ \boldsymbol{f_{A_y}} \end{bmatrix} = - \begin{bmatrix} \boldsymbol{C_\theta} & \boldsymbol{-S_\theta} \\ \boldsymbol{S_\theta} & \boldsymbol{C_\theta} \end{bmatrix} \begin{bmatrix} \boldsymbol{0} & \boldsymbol{0} \\ \boldsymbol{0} & \boldsymbol{\mu} \end{bmatrix} \begin{bmatrix} \boldsymbol{\dot{V}_{r_x}} \\ \boldsymbol{\dot{V}_{r_y}} \end{bmatrix} \tag{3.13}$$

where $\boldsymbol{\mu} = diag(\mu_1, ..., \mu_N) \in \mathbb{R}^{N\times N}$. The parameter μ_i is the added mass of each link. Since it is assumed that the underwater snake robot operates deeply submerged below the wave zone (assuming wave frequency going to zero), the added mass is assumed to have constant values.

The fluid torques on the links are given by Sverdrup-Thygeson et al. (2016b):

$$\boldsymbol{\tau} = -\boldsymbol{\Lambda_1}\ddot{\boldsymbol{\theta}} - \boldsymbol{\Lambda_2}\dot{\boldsymbol{\theta}} - \boldsymbol{\Lambda_3}\dot{\boldsymbol{\theta}}|\dot{\boldsymbol{\theta}}| \tag{3.14}$$

where $\boldsymbol{\Lambda_1} = diag(\lambda_{1,1}, ..., \lambda_{1,N}) \in \mathbb{R}^{N\times N}$, $\boldsymbol{\Lambda_2} = diag(\lambda_{2,1}, ..., \lambda_{2,N}) \in \mathbb{R}^{N\times N}$ and $\boldsymbol{\Lambda_3} = diag(\lambda_{3,1}, ..., \lambda_{3,N}) \in \mathbb{R}^{N\times N}$. The coefficient λ_1 represents the added mass parameter, while λ_2 and λ_3 represent the nonlinear and linear drag torque parameters, respectively.

In Kelasidi et al. (2014b) hydrodynamic parameters are given for the robot with identical links. The parameters are adjusted for an underwater snake robot with different links in Kelasidi et al. (2017). The cylindrical links have major diameter $2e_{1i}$, minor diameter $2e_{2i}$ and length of each link $2l_i$. The hydrodynamic related parameters are then given as

$$\begin{aligned} c_{T,i} &= \frac{1}{2}\rho\pi C_f \frac{(e_{2i}+e_{1i})}{2} 2l_i, \quad & c_{N,i} &= \frac{1}{2}\rho C_D 2e_{1i} 2l_i, \\ \mu_i &= \rho\pi C_A e_{1i}^2 2l_i, & \lambda_1, i &= \frac{1}{12}\rho\pi C_M (e_{1i}^2 - e_{2i}^2)^2 l_i^3, \\ \lambda_2, i &= \frac{1}{6}\rho\pi C_f (e_{1i}+e_{2i}) l_i^3, & \lambda_3, i &= \frac{1}{8}\rho\pi C_f (e_{1i}+e_{2i}) l_i^4 \end{aligned}$$

where C_f and C_D are the drag coefficients in the x and y direction, C_A is the added mass coefficient, C_M is the added inertia coefficient and ρ is the density of the fluid.

3.3 Forces from Added Effectors

The forces from added effectors along the snake robot are represented in Sverdrup-Thygeson et al. (2016b) and Kelasidi et al. (2017) as

$$\boldsymbol{f_{tx}} = \boldsymbol{B_x}^T \boldsymbol{f_t} \in \mathbb{R}^N, \qquad \boldsymbol{B_x}(\boldsymbol{b_x}) \in \mathbb{R}^{r \times N} \tag{3.15a}$$

$$\boldsymbol{f_{ty}} = \boldsymbol{B_y}^T \boldsymbol{f_t} \in \mathbb{R}^N, \qquad \boldsymbol{B_y}(\boldsymbol{b_y}) \in \mathbb{R}^{r \times N} \tag{3.15b}$$

where $\boldsymbol{b_x} = [cos(\theta_{k_1} + \zeta_{k_1}), cos(\theta_{k_2} + \zeta_{k_2}), ..., cos(\theta_{k_r} + \zeta_{k_r})]^T$ and $\boldsymbol{b_y} = [sin(\theta_{k_1} + \zeta_{k_1}), sin(\theta_{k_2} + \zeta_{k_2}), ..., sin(\theta_{k_r} + \zeta_{k_r})]^T$ are the x and y components of the added effector forces of link i. The parameter ζ_i represents the direction of the added effector in the local frame, while r describes the total number of additional effectors, $k_i \in (1, N)$. The force vectors $\boldsymbol{f_{tx}}$ and $\boldsymbol{f_{ty}}$ are given in the global frame.

The magnitude of the forces from the added effectors will be decreased as soon as the thrust losses are added. How the forces from the thrust losses are calculated is shown in Chapter 4.

3.4 Equations of Motion

The equations of motion are given in (3.16) and are found by using force balance using figure 3.2, as shown in Sverdrup-Thygeson et al. (2016b), Strømsøyen (2015) and Kelasidi et al. (2017).

$$\boldsymbol{M\ddot{X}} = \boldsymbol{D}^T \boldsymbol{h_x} + \boldsymbol{f_x} + \boldsymbol{f_{tx}}, \qquad \boldsymbol{M\ddot{Y}} = \boldsymbol{D}^T \boldsymbol{h_y} + \boldsymbol{f_y} + \boldsymbol{f_{ty}} \tag{3.16}$$

where $\boldsymbol{h_x}$ and $\boldsymbol{h_y}$ are given by (3.20).

The acceleration of the CM of the robot is given by Sverdrup-Thygeson et al. (2016b), Strømsøyen (2015), Kelasidi et al. (2017):

$$\begin{bmatrix} \ddot{p}_x \\ \ddot{p}_y \end{bmatrix} = \frac{1}{m_t} \begin{bmatrix} \boldsymbol{e}^T & \boldsymbol{0} \\ \boldsymbol{0} & \boldsymbol{e}^T \end{bmatrix} \begin{bmatrix} \boldsymbol{f_x} + \boldsymbol{f_{tx}} \\ \boldsymbol{f_y} + \boldsymbol{f_{ty}} \end{bmatrix} \tag{3.17}$$

By inserting (3.8), (3.11), (3.12), (3.6) and (3.7) into (3.17), the following equation for the acceleration of the CM of the robot is obtained.

$$\begin{aligned}\begin{bmatrix}\ddot{p}_x\\ \ddot{p}_y\end{bmatrix} =& -\boldsymbol{M_p N_p}\begin{bmatrix}diag(\dot{\boldsymbol{\theta}}) & \mathbf{0}\\ \mathbf{0} & diag(\dot{\boldsymbol{\theta}})\end{bmatrix}\boldsymbol{E}\begin{bmatrix}\dot{p}_x\\ \dot{p}_y\end{bmatrix}\\ &-\boldsymbol{M_p N_p}\begin{bmatrix}diag(\dot{\boldsymbol{\theta}}) & \mathbf{0}\\ \mathbf{0} & diag(\dot{\boldsymbol{\theta}})\end{bmatrix}\begin{bmatrix}\boldsymbol{K}^T\boldsymbol{S_\theta}\dot{\boldsymbol{\theta}}-\boldsymbol{V_x}\\ -\boldsymbol{K}^T\boldsymbol{C_\theta}\dot{\boldsymbol{\theta}}-\boldsymbol{V_y}\end{bmatrix}\\ &-\boldsymbol{M_p L_p}\begin{bmatrix}\boldsymbol{K}^T(\boldsymbol{C_\theta}\dot{\boldsymbol{\theta}}^2+\boldsymbol{S_\theta}\ddot{\boldsymbol{\theta}})\\ \boldsymbol{K}^T(\boldsymbol{S_\theta}\dot{\boldsymbol{\theta}}^2-\boldsymbol{C_\theta}\ddot{\boldsymbol{\theta}})\end{bmatrix}\\ &+\boldsymbol{M_p E}^T\begin{bmatrix}\boldsymbol{f_{D_x}}+\boldsymbol{f_{tx}}\\ \boldsymbol{f_{D_y}}+\boldsymbol{f_{ty}}\end{bmatrix}\end{aligned} \tag{3.18}$$

The matrices $\boldsymbol{M_p}$, $\boldsymbol{N_p}$ and $\mathbf{E}$ are given in Appendix A.

The torque balance equation is given by

$$\boldsymbol{J}\ddot{\theta} = \boldsymbol{D}^T\boldsymbol{u} - \boldsymbol{S_\theta L A}^T\boldsymbol{h_x} + \boldsymbol{C_\theta L A}^T\boldsymbol{h_y} + \boldsymbol{\tau} + \boldsymbol{\tau_t} \tag{3.19}$$

where $\mathbf{J}$ is given in Appendix A, $\boldsymbol{u} \in \mathbb{R}^{N-1}$ represents the control input, $\boldsymbol{\tau}$ is given by (3.14) and $\boldsymbol{\tau_t}$ represents the fluid torques given by the added effectors.

By multiplying (3.16) by $\mathbf{D}$ and solving for $\boldsymbol{h_x}$ and $\boldsymbol{h_y}$, the joint constraint forces are obtained as

$$\boldsymbol{h_x} = (\boldsymbol{D}\boldsymbol{D}^T)^{-1}\boldsymbol{D}(\boldsymbol{M}\ddot{\boldsymbol{X}} - \boldsymbol{f_x} - \boldsymbol{f_{tx}}) \tag{3.20a}$$

$$\boldsymbol{h_y} = (\boldsymbol{D}\boldsymbol{D}^T)^{-1}\boldsymbol{D}(\boldsymbol{M}\ddot{\boldsymbol{Y}} - \boldsymbol{f_y} - \boldsymbol{f_{ty}}) \tag{3.20b}$$

Inserting (3.20), (3.7) and (3.8) into (3.19), gives

$$
\begin{aligned}
&(\boldsymbol{J} + \boldsymbol{S_\theta V_1 S_\theta}) + \boldsymbol{C_\theta V_1 C_\theta}\ddot{\theta} - (-\boldsymbol{S_\theta V_1 C_\theta} + \boldsymbol{C_\theta V_1 S_\theta})\dot{\theta}^2 \\
&= \boldsymbol{D}^T\boldsymbol{u} - \boldsymbol{S_\theta V_2}\ddot{p}_x + \boldsymbol{C_\theta V_2}\ddot{p}_y + \boldsymbol{S_\theta V f_{A_x}} - \boldsymbol{C_\theta V f_{A_y}} \\
&+ \boldsymbol{S_\theta V}(\boldsymbol{f_{D_x}} + \boldsymbol{f_{tx}}) - \boldsymbol{C_\theta V}(\boldsymbol{f_{D_y}} + \boldsymbol{f_{ty}}) + \tau + \tau_{\boldsymbol{t}}
\end{aligned} \tag{3.21}
$$

where $\boldsymbol{V_1}$, $\boldsymbol{V_2}$ and $\boldsymbol{V}$ are found in Appendix A. The vectors $\boldsymbol{f_{Dx}} = \boldsymbol{f^I_{Dx}} + \boldsymbol{f^{II}_{Dx}}$ and $\boldsymbol{f_{Dy}} = \boldsymbol{f^I_{Dy}} + \boldsymbol{f^{II}_{Dy}}$ represents the drag forces in the x- and y-direction, respectively.

Finally, by inserting (3.13), (3.14) and (3.21) into (3.21), the rotational equation of motion of the underwater snake robot are represented as

$$
\begin{aligned}
&\boldsymbol{M_\theta}\ddot{\boldsymbol{\theta}} + \boldsymbol{W_\theta}\dot{\boldsymbol{\theta}}^{\boldsymbol{2}} + \boldsymbol{V_{\theta,\dot{\theta}}}\dot{\boldsymbol{\theta}} + \boldsymbol{N_{\theta,\dot{\theta}}}(\boldsymbol{e}\dot{p}_x - \boldsymbol{V_x}) + \boldsymbol{P_{\theta,\dot{\theta}}}(\boldsymbol{e}\dot{p}_y - \boldsymbol{V_y}) \\
&+ \boldsymbol{K_x}(\boldsymbol{f_{D_x}} + \boldsymbol{f_{tx}}) + \boldsymbol{K_y}(\boldsymbol{f_{D_y}} + \boldsymbol{f_{ty}}) - \tau_{\boldsymbol{t}} = \boldsymbol{D}^T\boldsymbol{u}
\end{aligned} \tag{3.22}
$$

where $\boldsymbol{M_\theta}$, $\boldsymbol{W_\theta}$, $\boldsymbol{V_{\theta,\dot{\theta}}}$, $\boldsymbol{N_{\theta,\dot{\theta}}}$, $\boldsymbol{V_x}$, $\boldsymbol{V_y}$, $\boldsymbol{K_x}$ and $\boldsymbol{K_y}$ are found in Appendix A.

Chapter 4

Propellers and Thrusters

The underwater snake robot with thrusters consists of two main propellers and tunnel thrusters along the body of the snake robot. All of these thrusters are the same type and are called T200 Thrusters. In this section, equations of nominal and actual thrust, torque and power will be recalled, as well as an explanation of the T200 Thrusters. The thruster dynamics will be explained, as well as different thrust losses and thruster controllers.

This chapter is primary based on Galta (2017), apart from Section 4.4.6.

4.1 Propeller Characteristics

The relationship between the actual propeller thrust (T_a), the actual propeller torque (Q_a), the actual propeller power consumption (P_a), shaft speed (n), diameter (D) and density of water (ρ) is given by

Carlton (2007):

$$T_a = sign(n) K_T \rho D^4 n^2 \tag{4.1a}$$

$$Q_a = sign(n) K_Q \rho D^5 n^2 \tag{4.1b}$$

$$P_a = 2\pi n Q_a = sign(n) 2\pi K_Q \rho D^5 n^3 \tag{4.1c}$$

where K_T and K_Q are strictly positive non-dimensional thrust and torque coefficients that accounts for the effects of thrust and torque losses. The expressions of these coefficients are found by open water tests. As described in Sørensen (2013), open water tests are usually performed in a cavitation tunnel or a towing tank. The actual thrust, actual torque and actual power shown above are affected by in-line velocity fluctuations only.

During open water tests, the relationship between the advance ratio J_a and the coefficients K_T and K_Q are found. This relationship is called open water characteristics. An example is shown in figure 4.1. According to Carlton (2007), open water characteristics relate to the description of the forces and moments acting on the propeller when operating in a uniform fluid stream which is parallel to the shaft center line.

The 1-quadrant model, covering positive shaft speeds and positive advance velocities, is being focused on in this text. To include negative advance ratios as well, the open-water characteristics should be extended to the 2^{nd} quadrant. In a complete 4-quadrant model, both positive and negative shaft speeds and advance ratios are covered.

The coefficients K_T, K_Q and J_a are defined as follows (Sørensen (2013), Carlton (2007), Lehn (1992)):

$$K_T = \frac{T_a}{\rho n^2 D^4} \tag{4.2}$$

$$K_Q = \frac{Q_a}{\rho n^2 D^5} \tag{4.3}$$

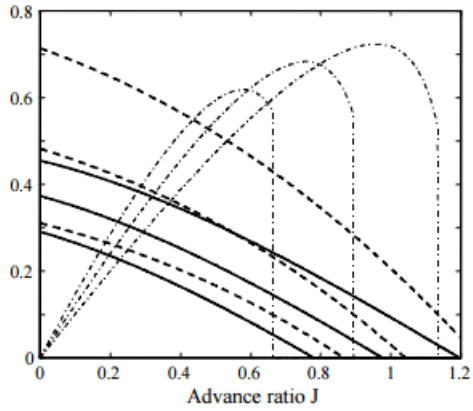

Figure 4.1: Example of open water characeristics found in Sørensen (2013). K_T is given by a solid line and $10 \cdot K_Q$ by a dashed line

$$J_a = \frac{V_a}{nD} \tag{4.4}$$

where V_a is the inflow velocity to the propeller and is given by Sørensen (2013):

$$V_a = U(1 - (w_w + w_p + w_v)) = U(1 - w). \tag{4.5}$$

The parameter U is the body speed and w is the *wake fraction number*. The *wake fraction number* accounts for the effect of the *wake*, which is the difference between the body speed U and the inflow velocity to the propeller V_a. w_w is the wake fraction caused by the wave motion of the water particles, w_p is the wake fraction caused by so called potential effects for a hull advancing forward in an ideal fluid and w_v is the wake fraction caused by viscous effects due to the effect of boundary layers. For ships, w is usually in the range of $0 < w < 0.4$. Deeply submerged underwater vehicles are not subjected to waves, hence w is assumed to be in the range of $0 < w < 0.1$.

A simplification of the 1^{st} quadrant propeller characteristics used in Blanke (1981), Blanke et al. (2000) and Fossen and Blanke (2000)

is shown below:

$$K_T = K_{T0} - \alpha_{T1} J_a \tag{4.6a}$$
$$K_Q = K_{Q0} - \alpha_{Q1} J_a \tag{4.6b}$$
$$T_a = T_{nn} n \mid n \mid - T_{nv} \mid n \mid V_a \tag{4.6c}$$
$$Q_a = Q_{nn} n \mid n \mid - Q_{nv} \mid n \mid V_a \tag{4.6d}$$

where K_{T0}, K_{Q0}, α_{T1} and α_{Q1} are constant coefficients for $V_a = 0$ and

$$T_{nn} = \rho D^4 K_{T0} \qquad T_{nv} = \rho D^3 \alpha_{T1}$$
$$Q_{nn} = \rho D^5 K_{Q0} \qquad Q_{nv} = \rho D^4 \alpha_{Q1}$$

This approximation is only for the 1^{st} quadrant. K_{T0} and K_{Q0} are the *nominal* thrust and torque coefficients for a deeply submerged propeller with $V_a = 0$ and no thrust losses. The corresponding nominal thrust, torque and power are expressed by:

$$T_n = sign(n) K_{T0} \rho D^4 n^2 \tag{4.7a}$$
$$Q_n = sign(n) K_{Q0} \rho D^5 n^2 \tag{4.7b}$$
$$P_n = 2\pi n Q_n = sign(n) 2\pi K_{Q0} \rho D^5 n^3 \tag{4.7c}$$

The actual propeller thrust and torque are T_a and Q_a, while the desired thrust and torque are T_n and Q_n, and are used as input in thruster controllers. Ideally they should be equal, but that is not realistic.

4.2 BlueRobotics T200 Thrusters

Both the main propellers and the thrusters along the snake body are BlueRobotics T200 Thrusters. The thrusters are shown in figure 4.2.

Figure 4.2: T2 Thrusters from BlueRobotics

Information about the dimensions and the performance of the thrusters are found in BlueRobotics (2017a) and BlueRobotics (2017b), and are shown in table 4.1.

Max thrust forward at 16 [V]	5.1 [kgf] = 50.01 [N]
Max thrust reverse at 16 [V]	4.1 [kgf] = 40.21 [N]
Max thrust forward at 12 [V]	3.55 [kgf] = 34.81 [N]
Max thrust reverse at 12 [V]	3.0 [kgf] = 29.42 [N]
Max rotational speed	3800 [RPM] = 63.33 [RPS]
Duct diameter	100 [mm]
Propeller diameter	76 [mm]

Table 4.1: Performance of the T200 Thrusters

4.3 Thruster Dynamics

Both the actuators and the drive system affect the thrust response. This leads to reduced actual thrust compared to desired thrust. When the frequency increases, the amplitude of the thrust decreases. The actual thrust will also be affected by disturbances in water inflow to the thruster blades by thruster-thruster interactions, thruster-hull in-

teractions, thruster-nearby structure interactions and ventilation, as well as current and vessel velocity. The thruster dynamics for each thruster is given by Sørensen (2013):

$$\dot{T}_a = -\frac{1}{T}(T_a + T_n) \tag{4.8}$$

where T is the time constant, T_a is the actual thrust and T_n is the nominal or desired thrust.

Solution of (4.8) follows from a standard ODE. For such a model, a solution of a proper time constant T for varying steps should be done.

4.4 Thrust Losses

In ideal conditions, a propeller would produce thrust and torque according to the nominal models. Any deviation of the nominal thrust and torque will in this thesis be defined as thrust losses.

This section focuses on six different thrust losses that will affect the underwater vehicle; in-line velocity fluctuations, transverse velocity fluctuations, thruster-thruster interactions, thruster-hull interactions, thruster-nearby structure interactions and ventilation. Losses from ventilation will only appear in the surface of the water. In-line velocity fluctuations and transverse velocity fluctuations will be simulated in MATLAB, while thruster-thruster interactions, thruster-hull interactions, thruster-nearby structure interactions and ventilation will be tested by a full scale model of the Eelume Underwater Snake Robot. Results from simulations and full scale testing are found in Chapter 5.

4.4.1 In-Line Velocity Fluctuations

Waves, currents and the vessel motion will induce a time-varying velocity field around the propeller. This can be decomposed in an in-line component and a transverse component as explained in Sørensen (2013). The in-line component will be affected by the current and

vessel motion in surge, sway and yaw, while the transverse component will be affected by the current and vessel motion in heave, roll and pitch.

The in-line, also called axial, component will give a change in the inflow velocity V_a, which also changes the advance ratio J_a as shown in (4.4). When J_a varies by time, the propeller operating point will move on the K_T- and K_Q-curves (see figure 4.1 for an example). This induces fluctuations in thrust, torque and power as shown in (4.1a), (4.1b) and (4.1c), respectively.

The thrust and torque loss factors, $\beta_{T,ax}$ and $\beta_{Q,ax}$ for a deeply submerged propeller, are given by Sørensen (2013) and Smogeli (2006):

$$\beta_{T,ax} = \frac{K_T(J_a)}{K_{T0}} \tag{4.9}$$

$$\beta_{Q,ax} = \frac{K_Q(J_a)}{K_{Q0}} \tag{4.10}$$

where K_{T0} and K_{Q0} are the nominal thrust and torque coefficients when $V_a = 0$.

4.4.2 Transverse Velocity Fluctuations

When the thruster operates in a current perpendicular to the propeller axis, a force in the direction of the current will be introduced to the thruster as explained in Lehn (1992). This force is due to the deflection of the propeller slipstream in the direction of the current and is called "cross-coupling drag". The force induce transverse velocity fluctuations.

For open and ducted propellers the force is given by Sørensen (2013)

$$F_t = K_{cc} D \sqrt{\rho T_a V_{tr}} \tag{4.11}$$

where K_{cc} is a cross-coupling drag factor and V_{tr} is the transverse velocity component. According to Sørensen (2013), the cross-coupling drag factor is usually set to 0.25 for ducted propellers and 0.31 for open propellers. The thrust loss factor $\beta_{T,tr}$ is given by

$$\beta_{T,tr} = 1 - \left(\frac{F_t}{T_a}\right)^2 = 1 - \left(\frac{K_{cc} D \sqrt{\rho T_a V_{tr}}}{T_a}\right)^2 = 1 - \rho K_{cc}^2 D^2 \frac{V_{tr}^2}{T_a}. \quad (4.12)$$

4.4.3 Thruster-Thruster Interactions

Thruster-thruster interactions occur when a thruster operates in a propeller slipstream of another thruster as explained in Lehn (1992). The source thruster develops a wake behind the propeller which gives an additional velocity to the inflow velocity of the affected propeller as shown in figure 4.3. This is described further in Faltinsen (2005), Carlton (2007), Schlichting (1979), Molland et al. (2011) and Steen (2014). The spread of the wake increases as the distance between the source propeller and the affected propeller becomes smaller. According to Steen (2014), momentum theory can be used to calculate the induced velocity of the wake.

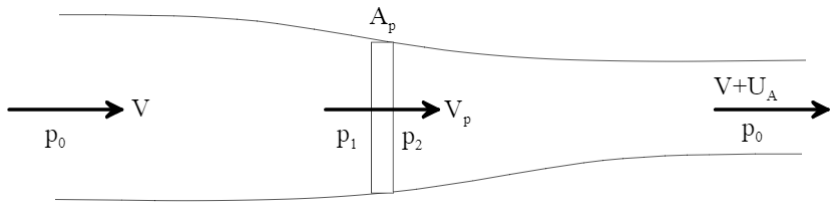

Figure 4.3: The parameter p_0 is the pressure far away, V is the robot's velocity, p_1 is the pressure right in front of the propeller, p_2 is the pressure right behind the propeller, V_p is the velocity at the propeller and U_A is the induced velocity given by the wake. Found in Steen (2014)

.

Thruster-thruster interactions can lead to considerable reduction of available thrust and propeller torque. Depending on the angle of the

propeller race relative to the thrust direction of the affected thruster, the propeller race may influence the neighboring thruster in several ways. Both in-line and transverse water inflow will be altered.

This thrust loss will occur when the snake robot is in a position where the thrusters are angled at each other, for example if the robot moves with lateral undulation.

4.4.4 Thruster-Hull Interactions

Thruster-hull interactions occur when the hull of the snake robot is located in the area of a propeller slipstream. The most important effect on the hull is the Coanda effect. This is when the propeller slip stream is attracted by the hull. When explaining the Coanda effect in Faltinsen (1990), the propeller slip stream is represented by a circular jet where the water is entrained from outside the jet. When a boundary (the hull) is present, there will be a resultant force from the jet towards the hull due to the pressure difference between the jet (high velocity, low pressure) and the hull (low velocity, high pressure). This force will attract the jet towards the hull as seen in figure 4.4.

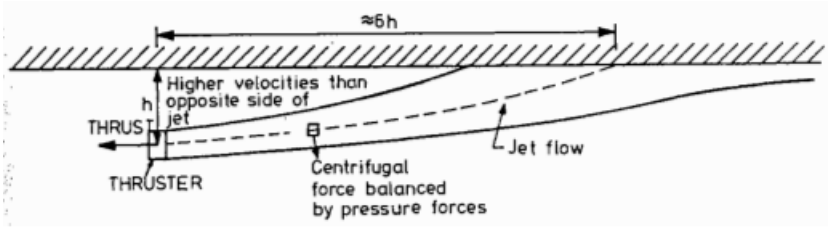

Figure 4.4: The Coanda effect from Faltinsen (1990).

This will affect the effects from the trust, and the movements of the snake body. The thrust will get a larger resistance than from the open water. Hence the thrust will give a larger effect to its link and move the link in a larger distance away from the hull it is affected by. The snake body will also be affected. The thrust will move the hull

further away from the thruster which may not be optimal.

This thrust loss can for example occur if the snake robot is formed as a circle in open water, or during transit when the main propellers are not located at the tail.

4.4.5 Thruster-Nearby Structure Interactions

Thruster-nearby structure interactions occur when a foreign structure is located in the area of a propeller slipstream. The thruster is affected approximately in the same way as in thruster-hull interactions, while the snake body is otherwise not affected. Low pressure will occur at the thruster because of high speed. It is assumed that the structure is at rest which leads to high pressure. A pressure difference between the thruster and the structure will occur which leads to a suction force that will attract the thruster to the hull.

If the nearby structure is fastened in some way, the thrust from the snake robot may lead to wear and tear of the structure. If the nearby structure is mobile, the thrust from the snake robot may both lead to wear and tear, as well as move the structure away from the snake robot.

This thrust loss can for example occur if the snake robot is near another structure to do investigation.

4.4.6 Ventilation

Ventilation is a phenomenon that may occur when the propeller is operating in the proximity of the free surface. According to Bernoulli's principle, the pressure at the propeller decreases when the velocity of the propeller increases. If the pressure at the propeller is lower than the atmospheric pressure, a suction might be created that sucks fluid from the region with high pressure (the air at the water surface) to the region with low pressure (where the propeller is located). This suction

looks like a funnel (or like the vortex that appear when you empty a sink or bathtub) which draws air from the free surface and through the propeller blade. The lower the pressure at the propeller is, the more likely it is that ventilation occurs. Ventilation is described in Sørensen (2013), Steen (2014), Faltinsen (1990) and Smogeli (2006). The loss is detectable due to sudden loss of thrust and increase of shaft speed and will lead to serious loss of propeller thrust and torque, and may damage the system.

Ventilation will not occur when the underwater snake robot operates deeply submerged in water. It will only occur when the underwater snake robot is near the water surface.

4.5 Thruster Control

A control system for the underwater snake robot is shown in figure 4.5. To control the thrusters of the USR, both a thruster controller and a thruster allocation are needed. The thruster controller is used to control the thrust to a desired value. Three controllers are described in the following: shaft speed controller, torque controller and power controller. Shaft speed controller or torque controller is usually used for underwater vehicles. The thruster allocation is needed to distribute the thrust wanted in each direction to each thruster. After the thruster allocation, the propeller characteristics such as losses are included and are given as inputs to the robot. The underwater snake robot moves and give data to the controller and so on. Normal conditions are assumed in the following sections.

4.5.1 Thruster Allocation

The thruster allocation receives the desired thrust in each direction $\tau = [\tau_x, \tau_y, \tau_z, \tau_\phi, \tau_\theta, \tau_\psi]^T$ and determines how much thrust each thruster of the vessel needs to produce.

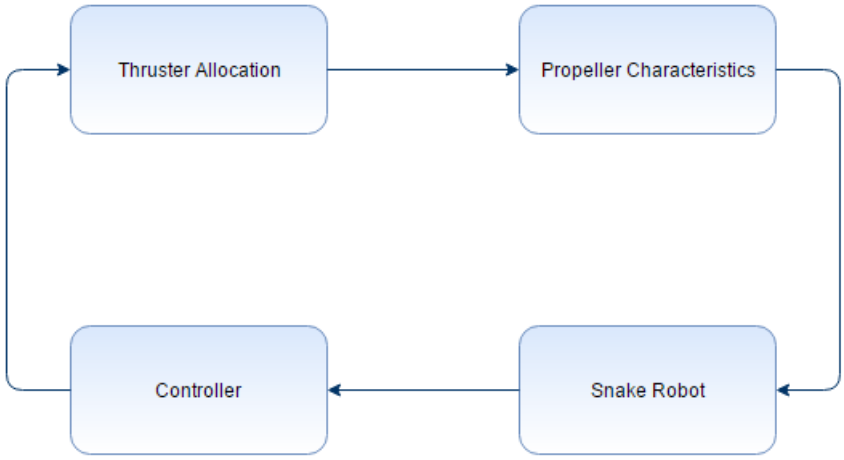

Figure 4.5: A control system of the underwater snake robot

As shown in Sørensen (2013), Fossen (2011), Sverdrup-Thygeson et al. (2016a) and Sverdrup-Thygeson et al. (2016b), the relationship between the control vector τ and the produced thrust from the r thrusters $\boldsymbol{T}_d$ is defined by

$$\boldsymbol{\tau} = \boldsymbol{T}(\boldsymbol{\alpha})\boldsymbol{T}_d = \boldsymbol{T}(\boldsymbol{\alpha})\boldsymbol{K}_{tr}\boldsymbol{u}_d \tag{4.13}$$

where $\boldsymbol{\alpha} = [\alpha_1, ..., \alpha_r]^T \in \mathbb{R}^r$ is a vector containing the azimuth angles and $\boldsymbol{T}(\boldsymbol{\alpha}) \in \mathbb{R}^{s \times r}$ is the thrust configuration matrix. The parameter s is the number of degrees of freedom (DOF) to be controlled and r is the number of thrusters. The thrust allocation matrix has one column vector for each actuator. The matrix $\boldsymbol{K}_{tr}$ is a matrix consisting of the thrust losses. If there are no thrust losses, the matrix will be the identity matrix. For a marine craft equipped with r actuators for operation in s DOFs, the thrust configuration matrix describes the geometry or locations of the actuators.

Thruster allocation for articulated structures is a complex dynamic problem, not only due to the dynamic response of the effectors, but also because the point of attack and line of action of the effector forces

change when the geometry of the USR is changed. The allocation matrix will thus be a function of the link angles. When the geometry of the USR is changed, the relative position and orientation of the thruster with respect to the base frame is also changed, which in turn changes the thruster configuration matrix. The configuration matrix will thus be a function of the joint angles.

When $r = s$, the USR is fully actuated and has the same amount of independent control inputs as degrees of freedom. When $r > s$, the USR is overactuated and have more actuators than degrees of freedom. Thus the thruster configuration is redundant, and secondary objectives can be included in the thruster allocation algorithm. Finally, when $r < s$, the USR is underactuated. This leads to the matrix becoming singular and non-invertible, and the thruster configuration matrix becomes rank deficient. Several marine applications are overactuated in order to ensure reliability.

4.5.2 Truster Controllers

Shaft Speed Control

A shaft speed controller is used when the shaft speed n is controlled to be equal to a desired speed n_d. A higher level controller has computed a desired thrust which is mapped to the corresponding revolution speed based on a thruster model. A PID controller is usually used with a shaft speed error $e = n_d - n$, and gives the commanded torque as shown below (Smogeli (2006))

$$Q_{cn} = K_p e + K_i \int_0^t e(\tau) d\tau + K_d \dot{e} \tag{4.14}$$

where $K_p > 0$, $K_i > 0$ and $K_d \geq 0$. The coefficient K_i is often given as $K_i = K_p/T_i$ where T_i is the integral time constant. To avoid integral windup, the integral term in the PID controller should be limited to some maximum Q_{max}, such as

$$|K_i \int_0^t e(\tau)d\tau| \leq Q_{i,max} \tag{4.15}$$

Torque Control

A torque controller is used when it is desired to keep the motor torque constant. In the torque control strategy the outer speed control loop is removed, and the thruster is controlled by its inner torque control loop with a commanded torque Q_{cq} as set-point. The commanded motor torque is set equal to the reference torque (Smogeli (2006)):

$$Q_{cq} = Q_r = \frac{K_{QC}}{K_{TC}} D T_a \tag{4.16}$$

where K_{QC} and K_{TC} are the control torque and thrust coefficients respectively.

Power Control

A power controller is used when the power consumption of the thruster motor is controlled. The inner loop from torque control is maintained, and the commanded torque Q_{cq} is calculated from the reference power P_r using feedback from the measured shaft speed n according to Smogeli (2006):

$$Q_{cp} = \frac{P_r}{2\pi|n|} = \frac{K_{QC}}{\sqrt{\rho} D K_{TC}^{3/2}} \frac{sign(T_a)|T_a|^{3/2}}{|n|} \qquad n \neq 0 \tag{4.17}$$

$$\tag{4.18}$$

Chapter 5

Simulations

In this chapter different thrust losses will be tested to verify which ones will give a distinct impact on the underwater snake robot's performance. In-line and transverse velocity fluctuations will be tested by simulations in MATLAB and are shown in Section 5.1. Thruster-thruster interactions, thruster-hull interactions, thruster-nearby structure interactions and ventilation will be tested by full scale testing of the model as seen in Section 5.2. The results will be discussed in Section 5.3.

The underwater snake robot will give the thrust calculated in (4.7a) in the ideal case where there are no thrust losses present. In reality there will always be a certain amount of thrust losses that affect the robot's performance. The actual thrust given from a thruster is

$$T_a = \beta_{il}\beta_{tr}\beta_{tt}\beta_{th}\beta_{tns}\beta_v T_n \tag{5.1}$$

were $\beta_{il} \in (0,1)$ is the factor that describes the impact on from the in-line velocity fluctuations, $\beta_{tr} \in (0,1)$ is the factor from transverse velocity fluctuations, $\beta_{tt} \in (0,1)$ is the factor from thruster-thruster interactions, $\beta_{th} \in (0,1)$ is the factor given by the thruster-hull interactions, $\beta_{tns} \in (0,1)$ is the factor from thruster-nearby structure interactions and $\beta_v \in (0,1)$ is the factor from ventilation. If the fac-

tors have no impact, they will be equal to one. Thus in the ideal case with no thrust losses, $T_a = T_n$.

5.1 Simulations in MATLAB

To study the effects from in-line velocity fluctuations and transverse velocity fluctuations, simulations are done to compare the cases with thrust losses to the nominal case in Section 5.1.1. The effect of different K_T-values are studied in Section 5.1.2, while current is added to the model in Section 5.1.3.

The underwater snake robot is straight in all of the following cases. Since this thesis is restricted for the robot to move in the horizontal 2D space, the vertical tunnel thrusters are neglected. A description of the input data is given in Appendix B and the MATLAB code is added in Appendix C. Five plots are given in each case; the path, the velocity in x- and y direction, the magnitude of the speed and the heading. All of these results are given for the global CM. Both low and high shaft speeds are tested. A shaft speed of $10[RPS]$ is added in the low speed cases, while the maximum shaft speed, $63[RPS]$, is added in the high speed cases. The advance ratio is assumed to be $J_a = 0.4$ in both cases. Both a small model and the actual model are tested. The small model uses the dimensions of the model originally used in the software code. This is a scaled model of the underwater snake robot without thrusters called Mamba, which is shown in figure 2.7. The actual model is the full size underwater snake robot with thrusters which is given in figure 2.8. The dimensions of the models are shown in table 5.1.

Model type	Weight per link	Length per link
Small model	$0.6597[kg]$	$70[mm]$
Actual model	$6[kg]$	$300[mm]$

Table 5.1: Dimensions of the small and the actual model

5.1.1 Comparing Nominal Thrust, In-Line Velocity Flucutations, and In-Line and Transverse Velocity Fluctuations

Four cases are studied in the following. Each case adds the thrust on different links and with different angles of attack. The figures compare how the underwater snake robot acts with nominal thrust, thrust with in-line velocity fluctuations and thrust with both in-line velocity fluctuations and transverse velocity fluctuations.

Case 1

The first case tests how the underwater snake robot responds to thrust given from the main propellers, which gives the robot forward speed.

Low speed

The shaft speed and angle of attack given from each thruster in case 1 with low speed are shown in table 5.2. Results from this simulation are shown in figure 5.1. The results from the small model are given on the left, while the results from the actual model are given on the right.

Link	1	2	3	4	5
Amplitude	0 [RPS]	0 [RPS]	10 [RPS]	0 [RPS]	0 [RPS]
Direction	0 [deg]	0 [deg]	0 [deg]	0 [deg]	0 [deg]

Table 5.2: Shaft speed and angle of attack for each thruster on the underwater snake robot when testing low speeds in case 1

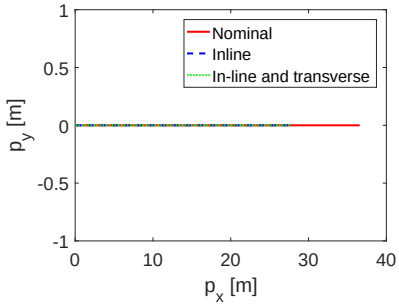

(a) Path of the robot using the small model

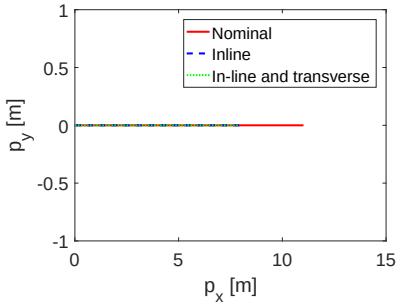

(b) Path of the robot using the actual model

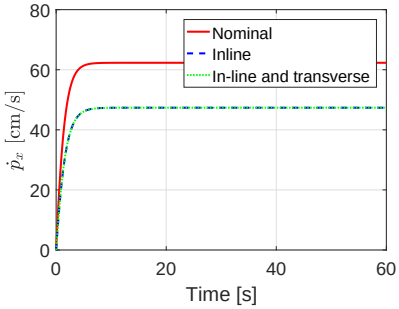

(c) Velocity in x-direction using the small model

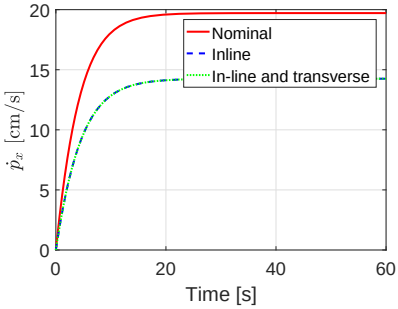

(d) Velocity in x-direction using the actual model

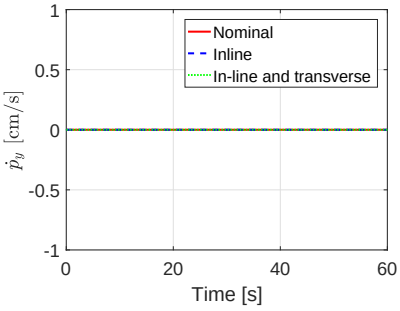

(e) Velocity in y-direction using the small model

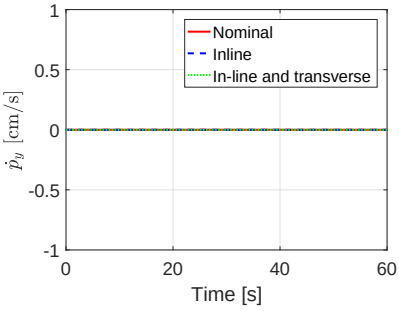

(f) Velocity in y-direction using the actual model

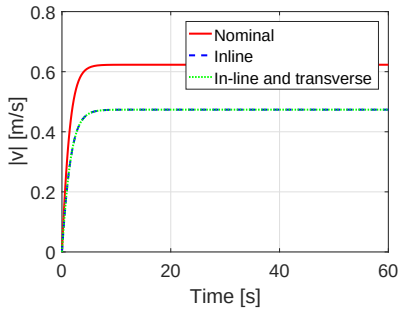

(g) Magnitude of the speed using the small model

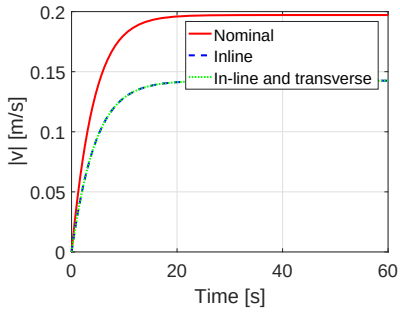

(h) Magnitude of the speed using the actual model

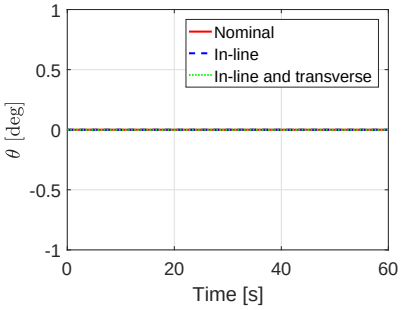

(i) Heading of the robot using the small model

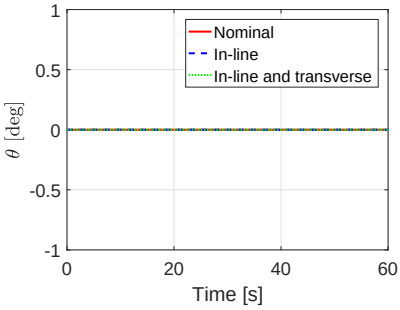

(j) Heading of the robot using the actual model

Figure 5.1: Tests done with low speed for case 1

High speed

The shaft speed and angle of attack given from each thruster in case 1 with high speed are shown in table 5.3. Results from this simulation are shown in figure 5.2. The results from the small model are given on the left, while the results from the actual model are given on the right.

Link	1	2	3	4	5
Amplitude	0 [RPS]	0 [RPS]	63 [RPS]	0 [RPS]	0 [RPS]
Direction	0 [deg]	0 [deg]	0 [deg]	0 [deg]	0 [deg]

Table 5.3: Shaft speed and angle of attack for each thruster on the underwater snake robot when testing high speeds in case 1

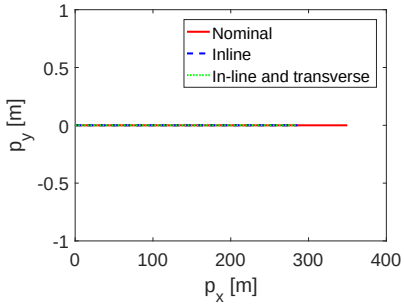

(a) Path of the robot using the small model

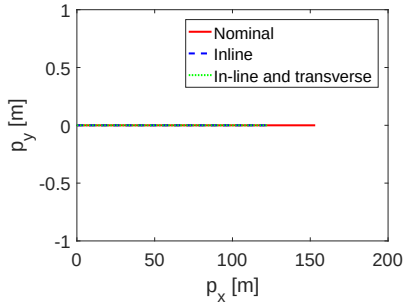

(b) Path of the robot using the actual model

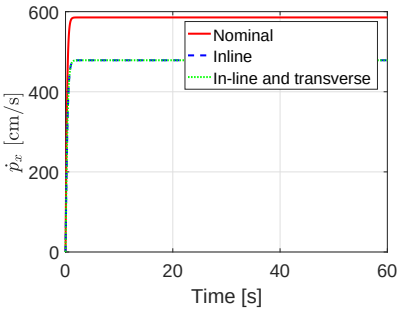

(c) Velocity in x-direction using the small model

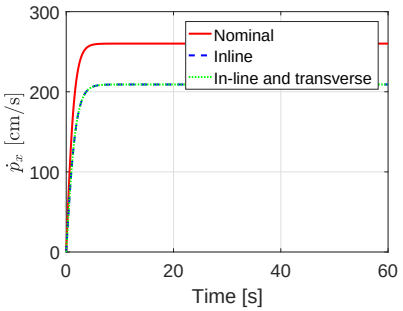

(d) Velocity in x-direction using the actual model

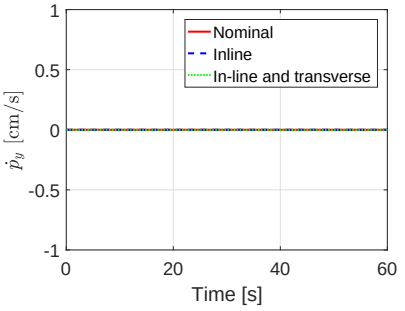

(e) Velocity in y-direction using the small model

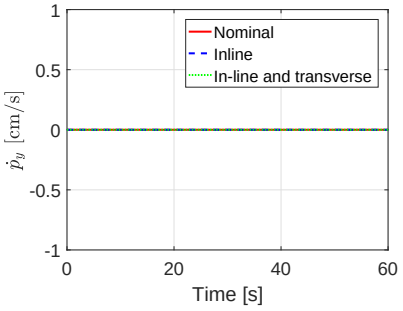

(f) Velocity in y-direction using the actual model

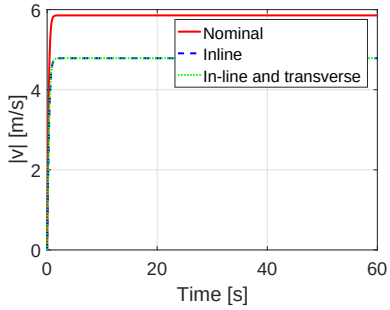

(g) Magnitude of the speed using the small model

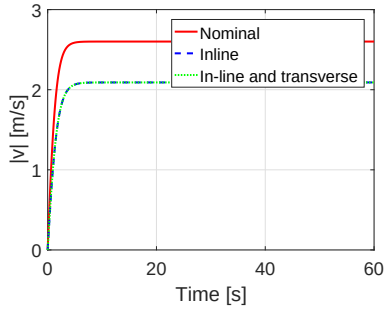

(h) Magnitude of the speed using the actual model

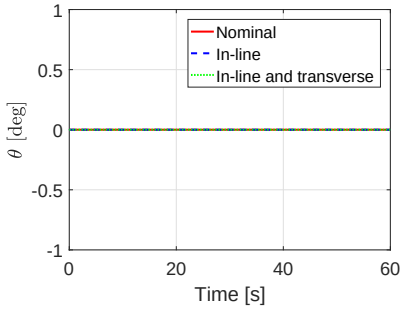

(i) Heading of the robot using the small model

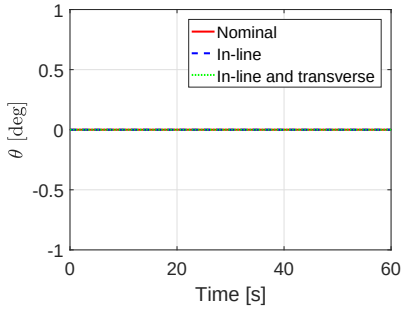

(j) Heading of the robot using the actual model

Figure 5.2: Tests done with high speed for case 1

Case 2

The second case tests how the underwater snake robot responds to thrust given from one of the tunnel thrusters, which gives the robot sideways speed and will make the robot turn in circle.

Low speed

The shaft speed and angle of attack given from each thruster in case 2 with low speed are shown in table 5.4. Results from this simulation are shown in figure 5.3. The results from the small model are given on the left, while the results from the actual model are given on the

right.

Link	1	2	3	4	5
Amplitude	0 [RPS]	10 [RPS]	0 [RPS]	0 [RPS]	0 [RPS]
Direction	0 [deg]	90 [deg]	0 [deg]	0 [deg]	0 [deg]

Table 5.4: Shaft speed and angle of attack for each thruster on the underwater snake robot when testing low speeds in case 2

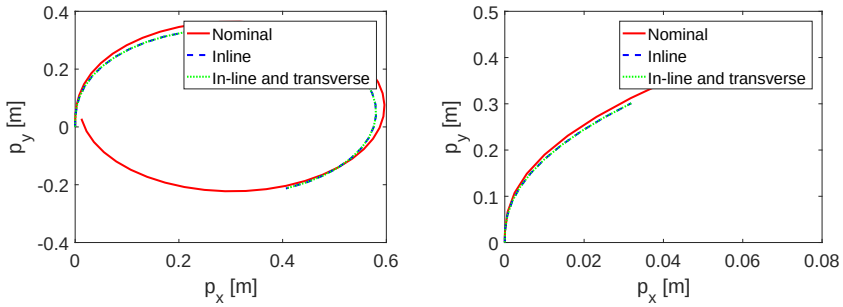

(a) Path of the robot using the small model

(b) Path of the robot using the actual model

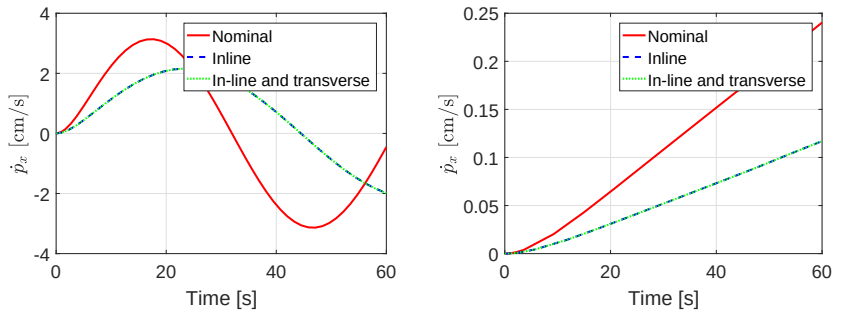

(c) Velocity in x-direction using the small model

(d) Velocity in x-direction using the actual model

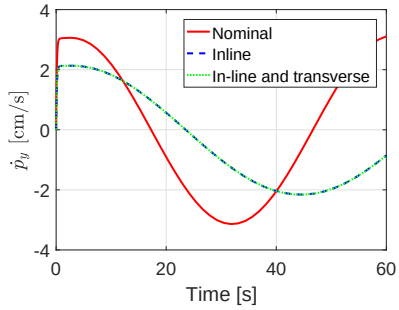

(e) Velocity in y-direction using the small model

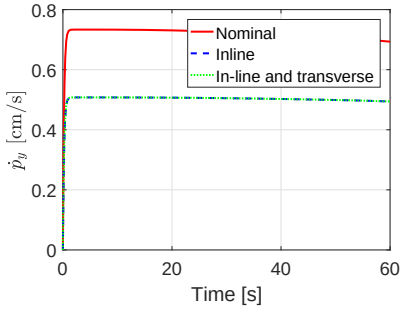

(f) Velocity in y-direction using the actual model

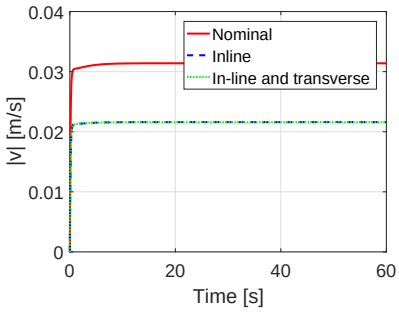

(g) Magnitude of the speed using the small model

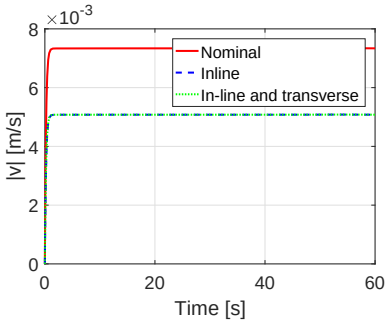

(h) Magnitude of the speed using the actual model

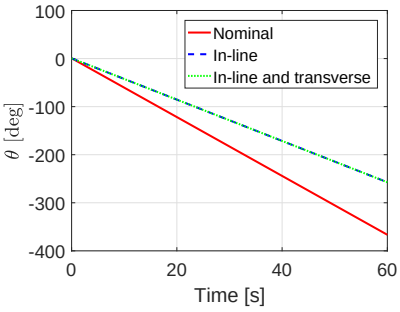

(i) Heading of the robot using the small model

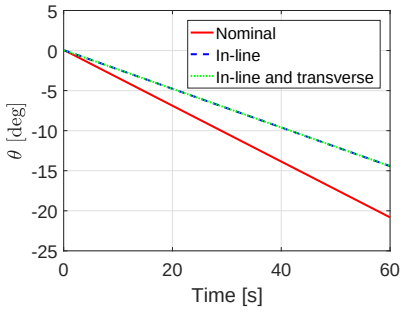

(j) Heading of the robot using the actual model

Figure 5.3: Tests done with low speed for case 2

High speed

The shaft speed and angle of attack given from each thruster in case 2 with high speed are shown in table 5.5. Results from this simulation are shown in figure 5.4. The results from the small model are given on the left, while the results from the actual model are given on the right.

Link	1	2	3	4	5
Amplitude	0 [RPS]	63 [RPS]	0 [RPS]	0 [RPS]	0 [RPS]
Direction	0 [deg]	90 [deg]	0 [deg]	0 [deg]	0 [deg]

Table 5.5: Shaft speed and angle of attack for each thruster on the underwater snake robot when testing high speeds in case 2

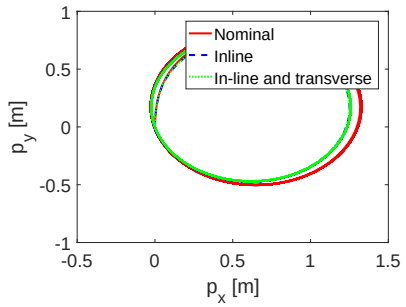

(a) Path of the robot using the small model

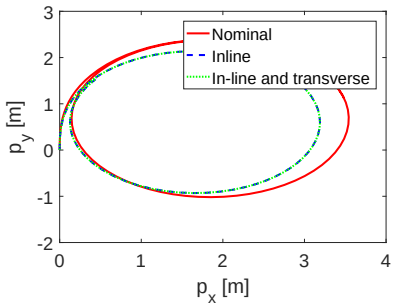

(b) Path of the robot using the actual model

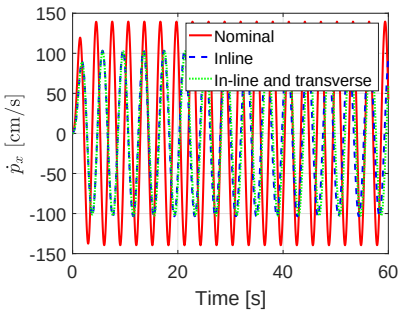

(c) Velocity in x-direction using the small model

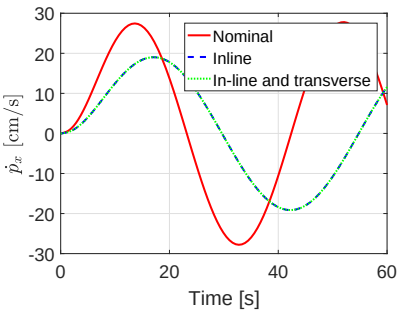

(d) Velocity in x-direction using the actual model

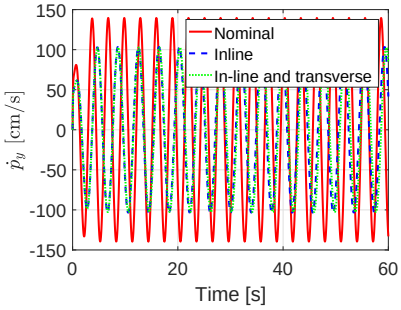

(e) Velocity in y-direction using the small model

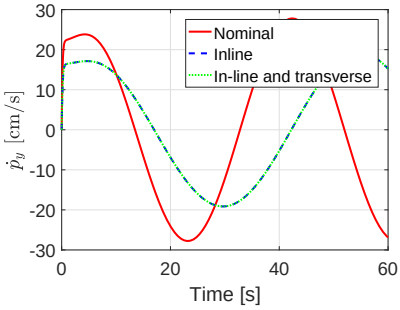

(f) Velocity in y-direction using the actual model

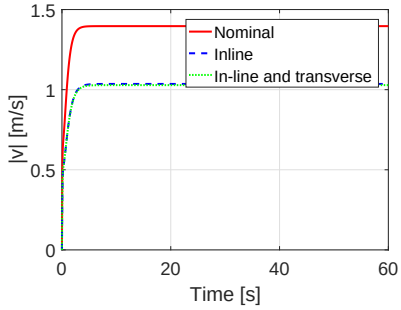

(g) Magnitude of the speed using the small model

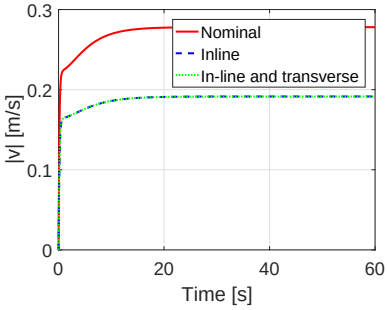

(h) Magnitude of the speed using the actual model

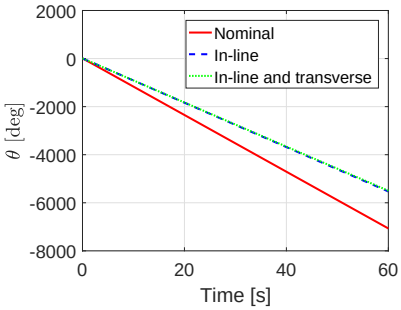

(i) Heading of the robot using the small model

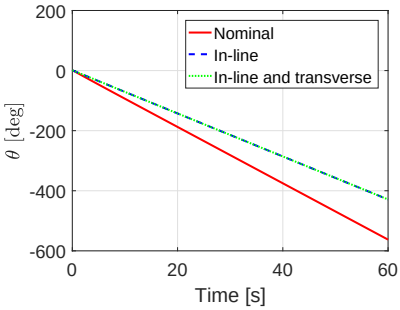

(j) Heading of the robot using the actual model

Figure 5.4: Tests done with high speed for case 2

Case 3

The third case tests how the underwater snake robot responds to thrust given from both the main propellers and one of the tunnel thrusters, which will make the robot turn while giving a forward speed as well.

Low speed

The shaft speed and angle of attack given from each thruster in case 3 with low speed are shown in table 5.6. Results from this simulation are shown in figure 5.5. The results from the small model are given on the left, while the results from the actual model are given on the right.

Link	1	2	3	4	5
Amplitude	0 [RPS]	10 [RPS]	10 [RPS]	0 [RPS]	0 [RPS]
Direction	0 [deg]	90 [deg]	0 [deg]	0 [deg]	0 [deg]

Table 5.6: Shaft speed and angle of attack for each thruster on the underwater snake robot when testing low speeds in case 3

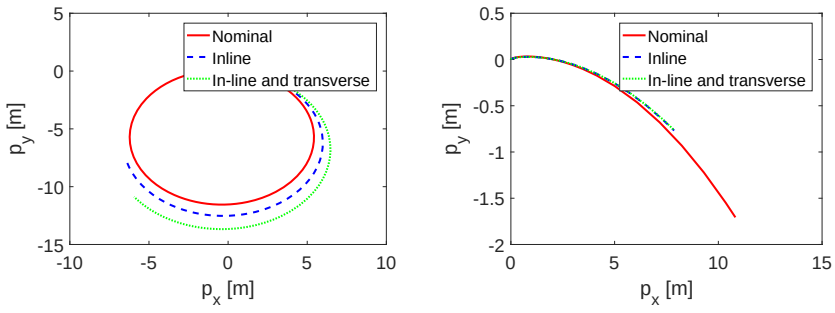

(a) Path of the robot using the small model

(b) Path of the robot using the actual model

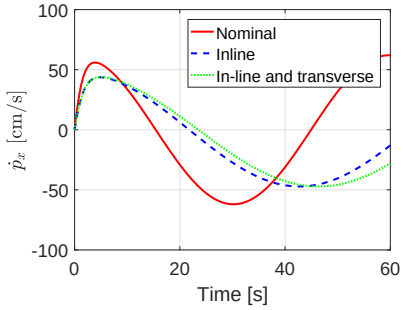

(c) Velocity in x-direction using the small model

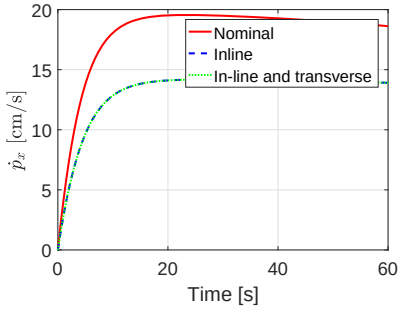

(d) Velocity in x-direction using the actual model

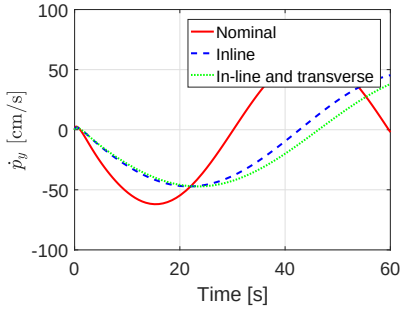

(e) Velocity in y-direction using the small model

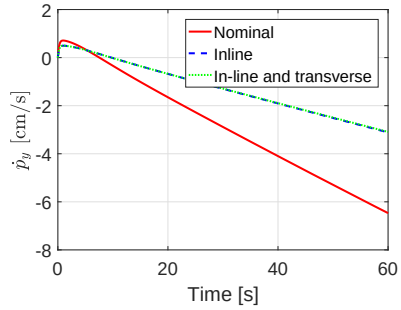

(f) Velocity in y-direction using the actual model

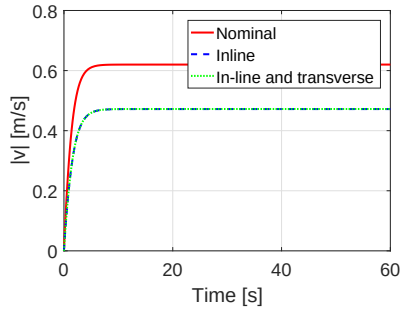

(g) Magnitude of the speed using the small model

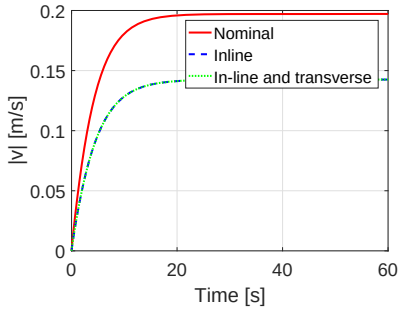

(h) Magnitude of the speed using the actual model

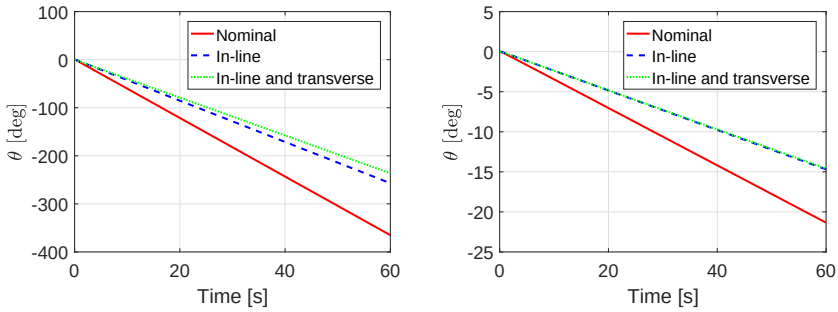

(i) Heading of the robot using the small model

(j) Heading of the robot using the actual model

Figure 5.5: Tests done with low speed for case 3

High speed

The shaft speed and angle of attack given from each thruster in case 3 with high speed are shown in table 5.7. Results from this simulation are shown in figure 5.6. The results from the small model are given on the left, while the results from the actual model are given on the right.

Link	1	2	3	4	5
Amplitude	0 [RPS]	63 [RPS]	63 [RPS]	0 [RPS]	0 [RPS]
Direction	0 [deg]	90 [deg]	0 [deg]	0 [deg]	0 [deg]

Table 5.7: Shaft speed and angle of attack for each thruster on the underwater snake robot when testing high speeds in case 3

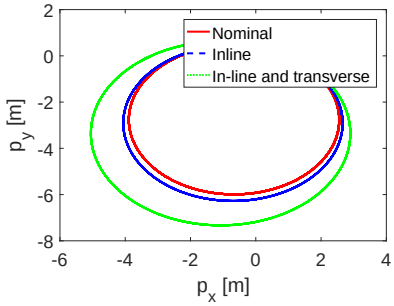

(a) Path of the robot using the small model

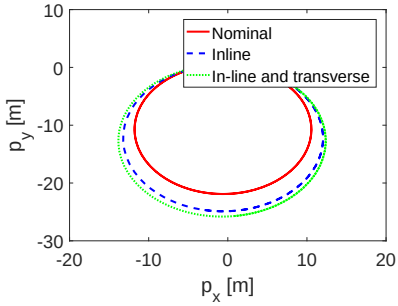

(b) Path of the robot using the actual model

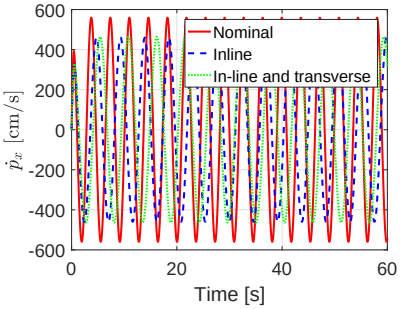

(c) Velocity in x-direction using the small model

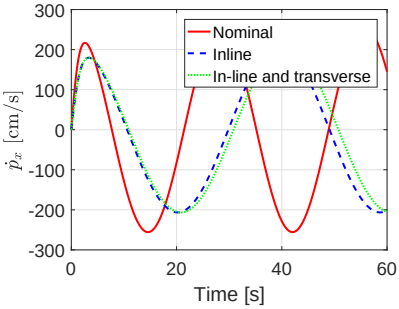

(d) Velocity in x-direction using the actual model

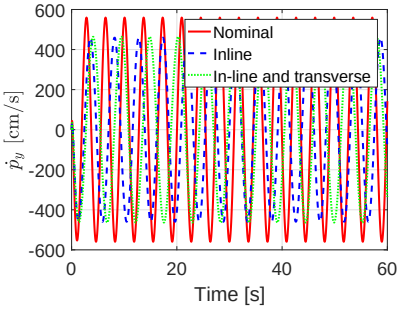

(e) Velocity in y-direction using the small model

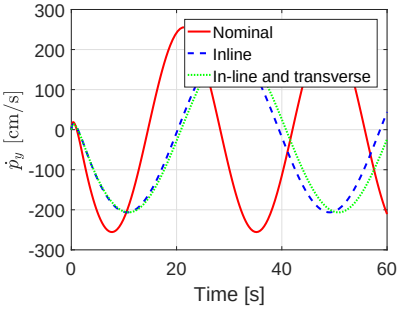

(f) Velocity in y-direction using the actual model

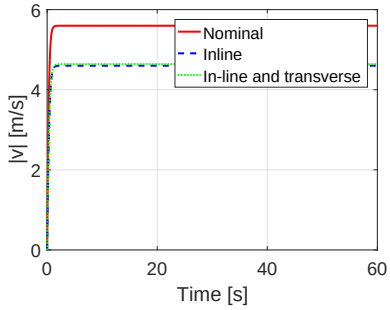

(g) Magnitude of the speed using the small model

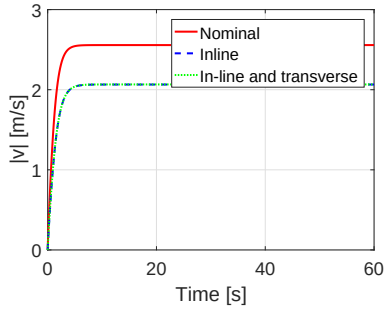

(h) Magnitude of the speed using the actual model

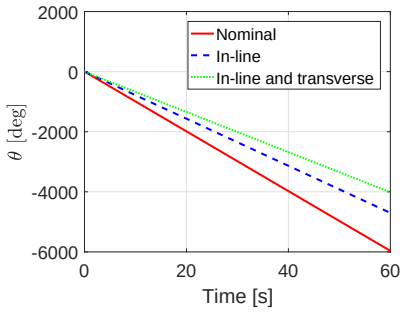

(i) Heading of robot using the small model

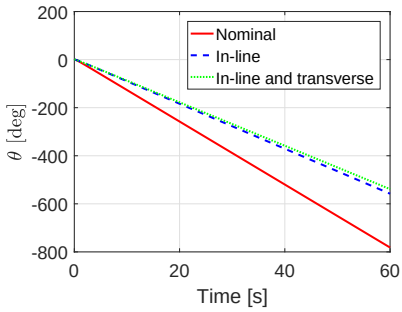

(j) Heading of robot using the actual model

Figure 5.6: Tests done with high speed for case 3

Case 4

The fourth case tests how the underwater snake robot responds to thrust given from the thruster in link 3 with an angle of 15°.

Low speed

The shaft speed and angle of attack given from each thruster in case 4 with low speed are shown in table 5.8. Results from this simulation are shown in figure 5.7. The results from the small model are given on the left, while the results from the actual model are given on the right.

Link	1	2	3	4	5
Amplitude	0 [RPS]	0 [RPS]	10 [RPS]	0 [RPS]	0 [RPS]
Direction	0 [deg]	0 [deg]	15 [deg]	0 [deg]	0 [deg]

Table 5.8: Shaft speed and angle of attack for each thruster on the underwater snake robot when testing low speeds in case 4

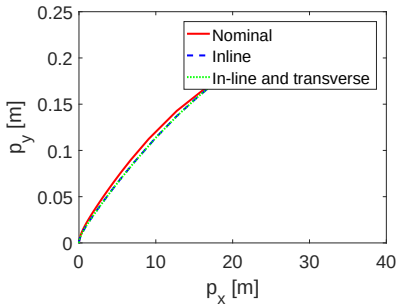

(a) Path of the robot using the small model

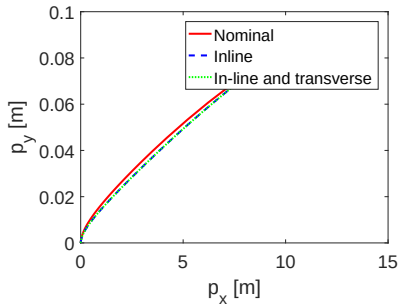

(b) Path of the robot using the actual model

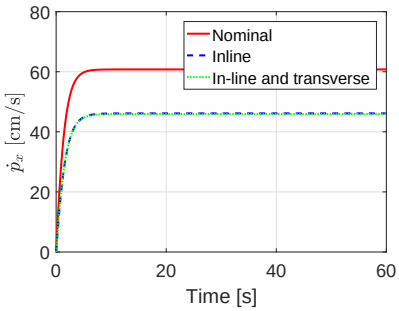

(c) Velocity in x-direction using the small model

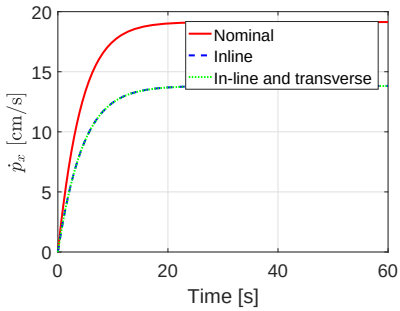

(d) Velocity in x-direction using the actual model

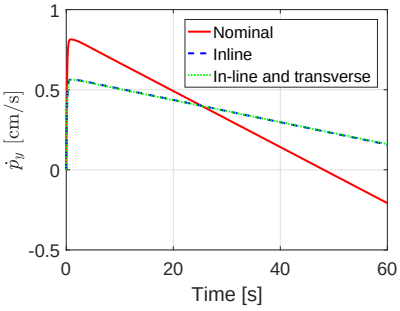

(e) Velocity in y-direction using the small model

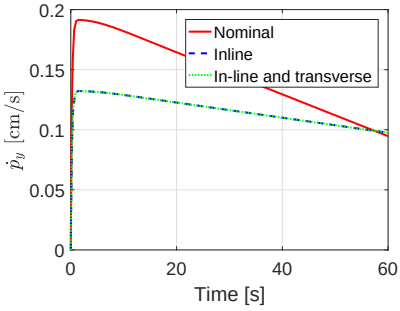

(f) Velocity in y-direction using the actual model

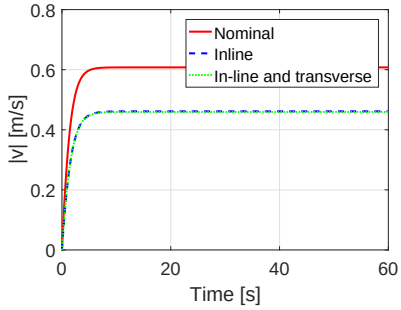

(g) Magnitude of the speed using the small model

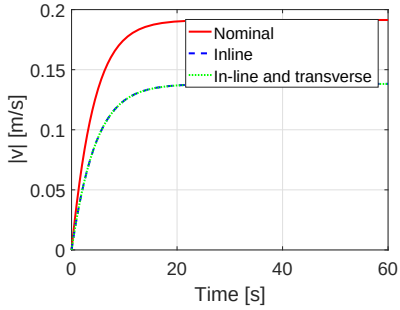

(h) Magnitude of the speed using the actual model

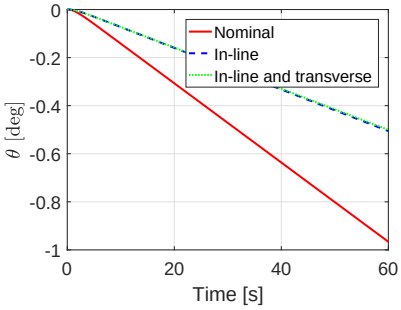

(i) Heading of the robot using the small model

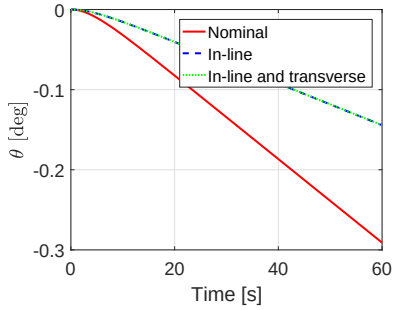

(j) Heading of the robot using the actual model

Figure 5.7: Tests done with low speed for case 4

High speed

The shaft speed and angle of attack given from each thruster in case 4 with high speed are shown in table 5.9. Results from this simulation are shown in figure 5.8. The results from the small model are given on the left, while the results from the actual model are given on the right.

Link	1	2	3	4	5
Amplitude	0 [RPS]	0 [RPS]	63 [RPS]	0 [RPS]	0 [RPS]
Direction	0 [deg]	0 [deg]	15 [deg]	0 [deg]	0 [deg]

Table 5.9: Shaft speed and angle of attack for each thruster on the underwater snake robot when testing high speeds in case 4

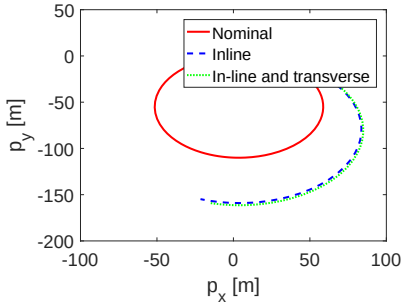

(a) Path of the robot using the small model

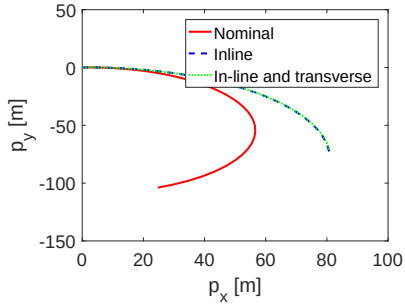

(b) Path of the robot using the actual model

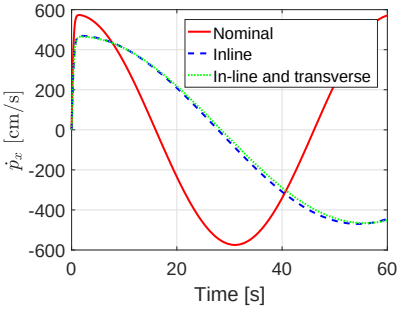

(c) Velocity in x-direction using the small model

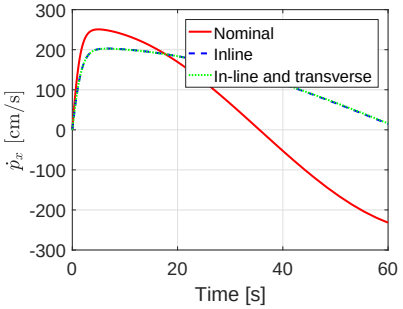

(d) Velocity in x-direction using the actual model

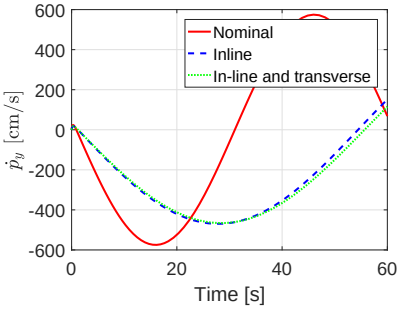

(e) Velocity in y-direction using the small model

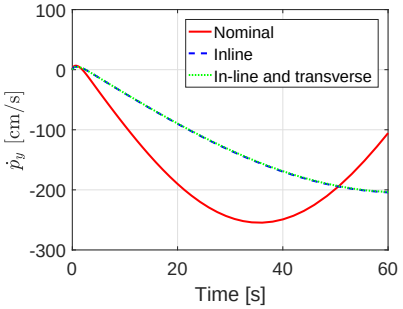

(f) Velocity in y-direction using the actual model

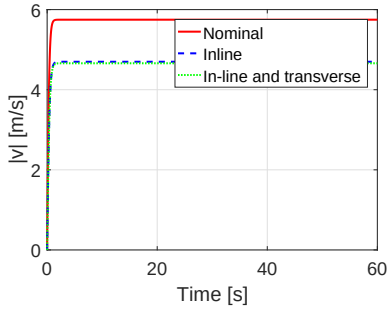

(g) Magnitude of the speed using the small model

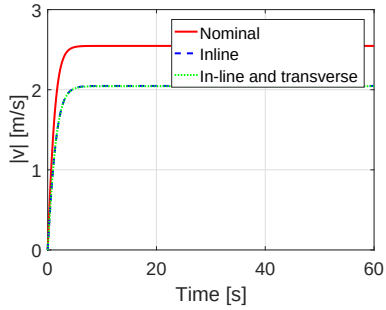

(h) Magnitude of the speed using the actual model

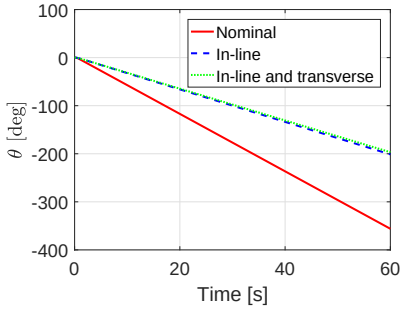

(i) Heading of the robot using the small model

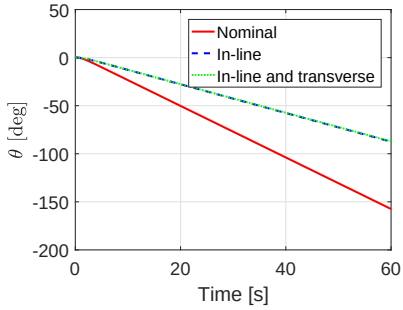

(j) Heading of the robot using the actual model

Figure 5.8: Tests done with high speed for case 4

5.1.2 The Influence of K_T

In this section the influence of K_T is studied by testing different K_T-values. Using (B.3a), the K_T-values are calculated by using different values for J_a as shown in table 5.10.

i	0	1	2	3	4
$J_{a,i}$	0	0.2	0.4	0.6	0.8
$K_{T,i}$	0.4000	0.3440	0.2760	0.1960	0.1040

Table 5.10: Different K_T-values for each J_a-value

In the following simulations, thrust in both the main propellers and in one tunnel thruster is added. The results from the small model are given on the left, while the results from the actual model are given on the right. The figures compare how the underwater snake robot acts with different K_T-values.

Low Speed

The shaft speed and angle of attack given from each thruster are shown in table 5.11. Results from this simulation are shown in figure 5.9. The results from the small model are given on the left, while the results from the actual model are given on the right.

Link	1	2	3	4	5
Amplitude	0 [RPS]	10 [RPS]	10 [RPS]	0 [RPS]	0 [RPS]
Direction	0 [deg]	90 [deg]	0 [deg]	0 [deg]	0 [deg]

Table 5.11: Shaft speed and angle of attack for each thruster when testing K_T-values with low speed

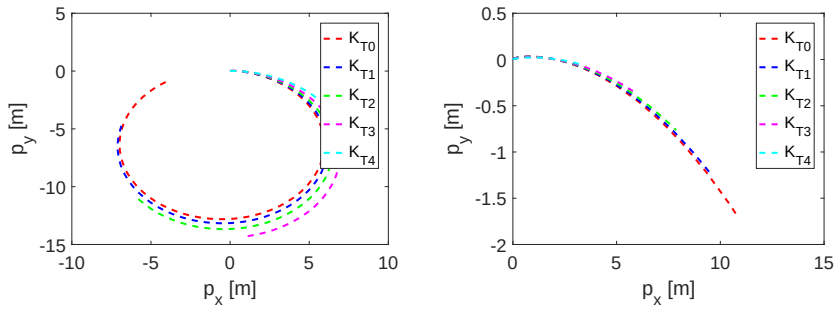

(a) Path of the robot using the small model

(b) Path of the robot using the actual model

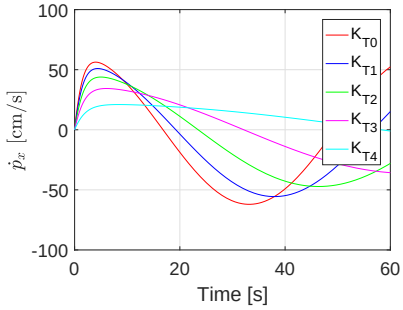

(c) Velocity in x-direction using the small model

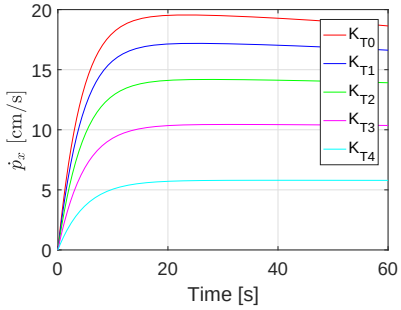

(d) Velocity in x-direction using the actual model

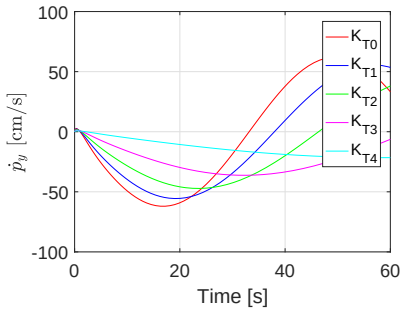

(e) Velocity in y-direction using the small model

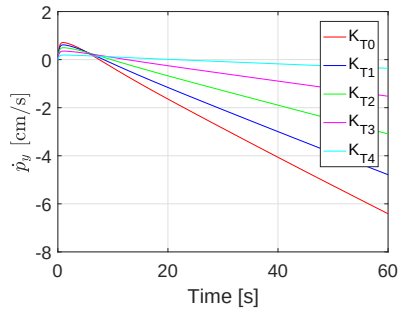

(f) Velocity in y-direction using the actual model

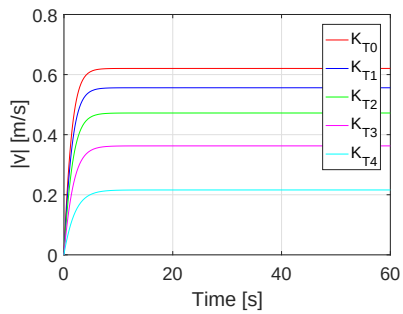

(g) Magnitude of the speed using the small model

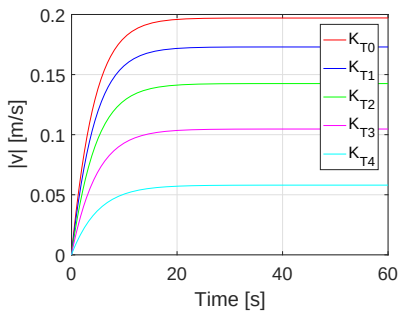

(h) Magnitude of the speed using the actual model

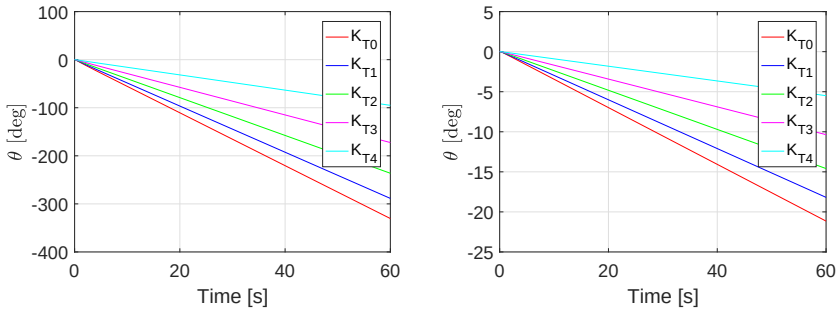

(i) Heading of the robot using the small model

(j) Heading of the robot using the actual model

Figure 5.9: Tests done to test the influence of K_T in low speeds

High Speed

The shaft speed and angle of attack given from each thruster are shown in table 5.12. Results from this simulation are shown in figure 5.10. The results from the small model are given on the left, while the results from the actual model are given on the right.

Link	1	2	3	4	5
Amplitude	0 [RPS]	63 [RPS]	63 [RPS]	0 [RPS]	0 [RPS]
Direction	0 [deg]	90 [deg]	0 [deg]	0 [deg]	0 [deg]

Table 5.12: Shaft speed and angle of attack for each thruster when testing K_T-values with high speed

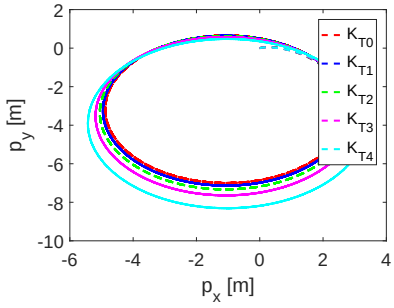

(a) Path of the robot using the small model

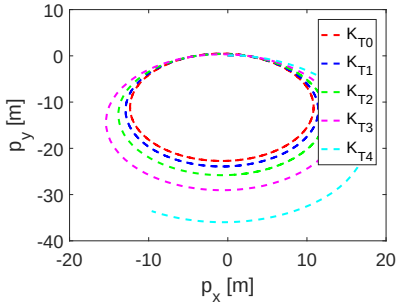

(b) Path of the robot using the actual model

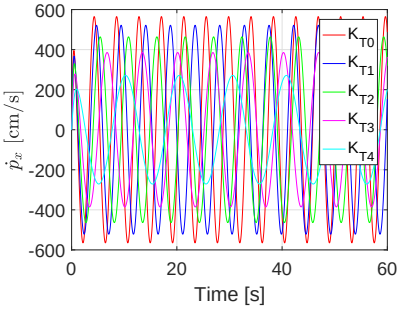

(c) Velocity in x-direction using the small model

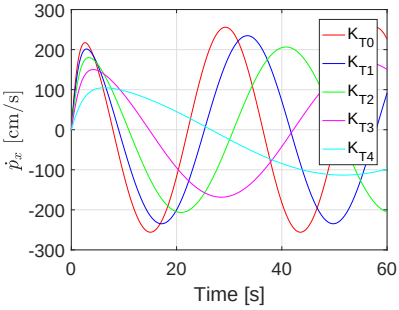

(d) Velocity in x-direction using the actual model

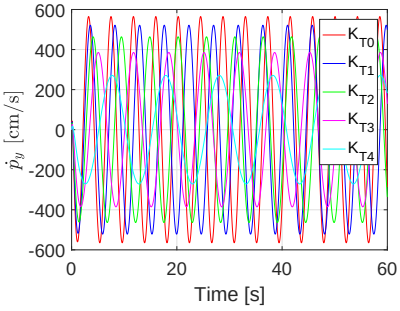

(e) Velocity in y-direction using the small model

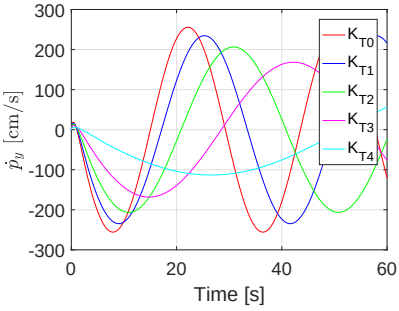

(f) Velocity in y-direction using the actual model

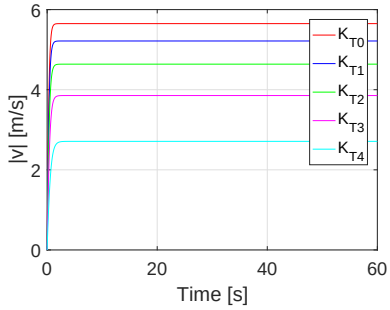

(g) Magnitude of the speed using the small model

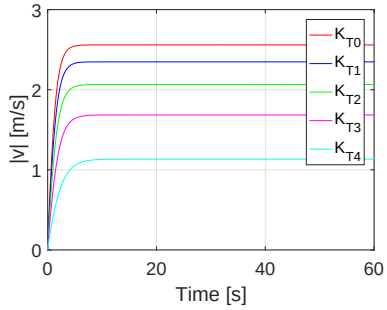

(h) Magnitude of the speed using the actual model

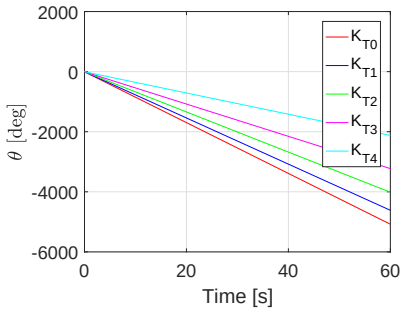

(i) Heading of the robot using the small model

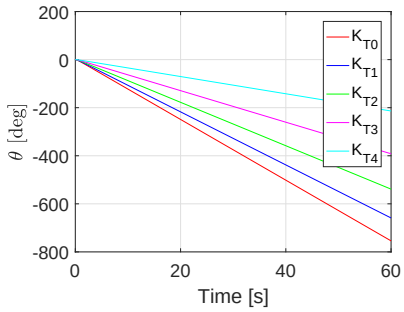

(j) Heading of the robot using the actual model

Figure 5.10: Tests done to test the influence of K_T in high speeds

5.1.3 Adding Current

In this section, current is added to the model to test if the thrust-loss model added by the author corresponds with the current. A current of $0.1[m/s]$ is given in the global x-direction, while a current of $-0.1[m/s]$ is given in the global y-direction. Thrust is given from the tunnel thruster in link two.

Low Speed

The shaft speed and angle of attack given from each thruster are shown in table 5.13. Results from this simulation are shown in figure

5.11. The results from the small model are given on the left, while the results from the actual model are given on the right.

Link	1	2	3	4	5
Amplitude	0 [RPS]	10 [RPS]	0 [RPS]	0 [RPS]	0 [RPS]
Direction	0 [deg]	90 [deg]	0 [deg]	0 [deg]	0 [deg]

Table 5.13: Shaft speed and angle of attack for each thruster when testing the underwater snake robot on low speeds in current

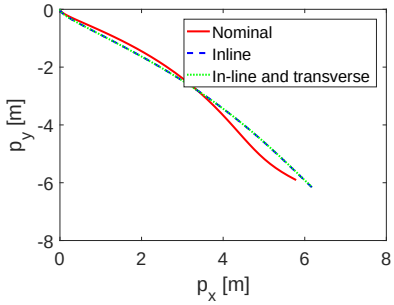

(a) Path of the robot using the small model

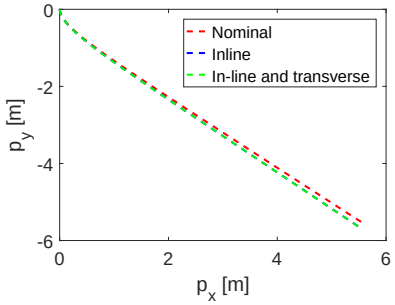

(b) Path of the robot using the actual model

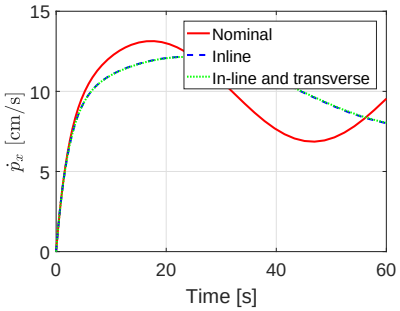

(c) Velocity in x-direction using the small model

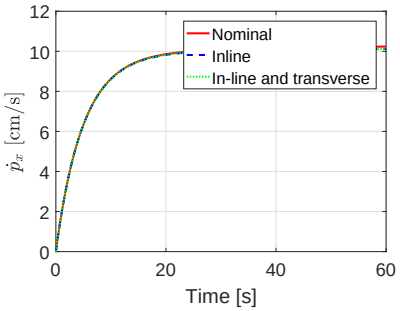

(d) Velocity in x-direction using the actual model

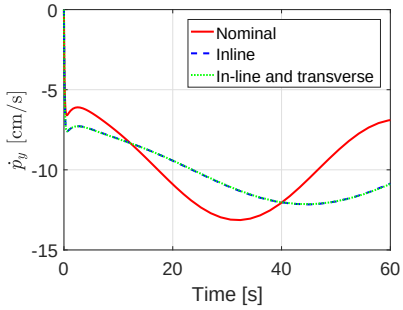

(e) Velocity in y-direction using the small model

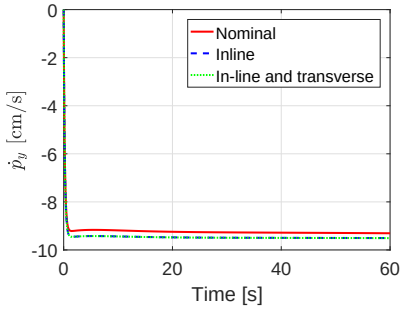

(f) Velocity in y-direction using the actual model

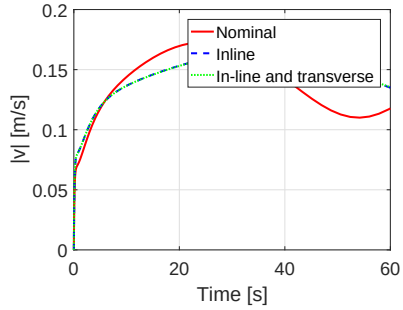

(g) Magnitude of the speed using the small model

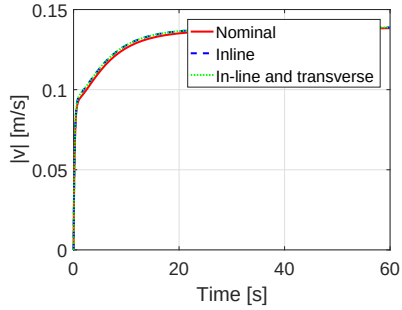

(h) Magnitude of the speed using the actual model

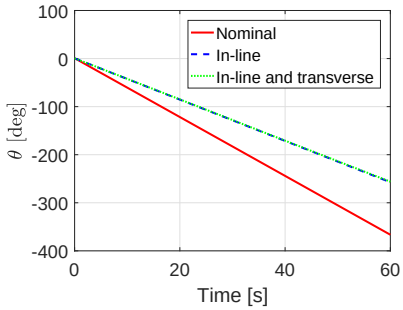

(i) Heading of the robot using the small model

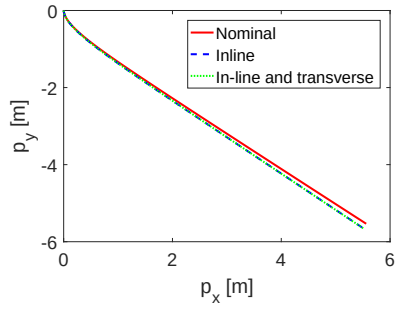

(j) Heading of the robot using the actual model

Figure 5.11: Tests done to study the performance of the underwater snake robot with low speeds in current

High Speed

The shaft speed and angle of attack given from each thruster are shown in table 5.14. Results from this simulation are shown in figure 5.12. The results from the small model are given on the left, while the results from the actual model are given on the right.

Link	1	2	3	4	5
Amplitude	0 [RPS]	63 [RPS]	0 [RPS]	0 [RPS]	0 [RPS]
Direction	0 [deg]	90 [deg]	0 [deg]	0 [deg]	0 [deg]

Table 5.14: Shaft speed and angle of attack for each thruster when testing the underwater snake robot on high speeds in current

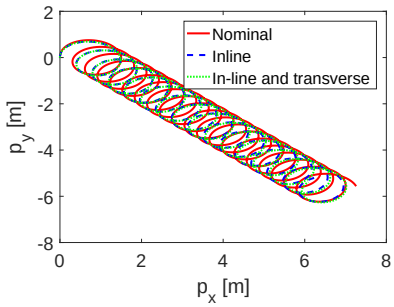

(a) Path of the robot using the small model

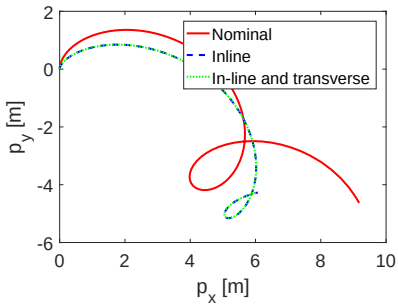

(b) Path of the robot using the actual model

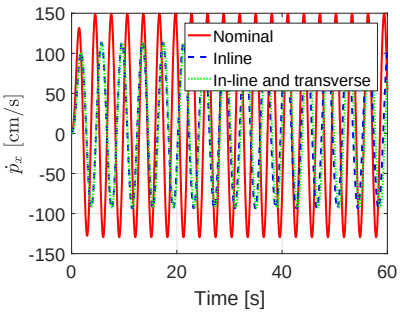

(c) Velocity in x-direction using the small model

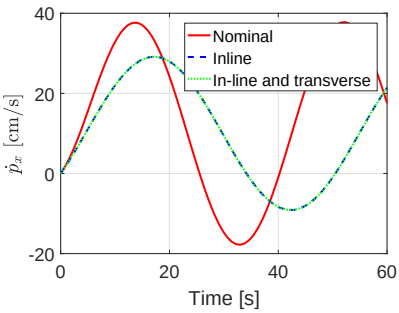

(d) Velocity in x-direction using the actual model

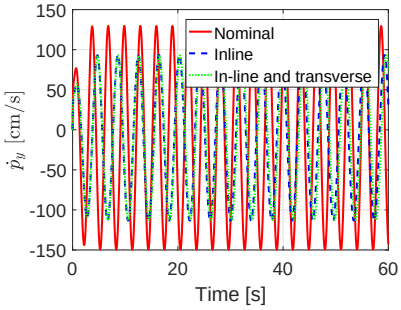

(e) Velocity in y-direction using the small model

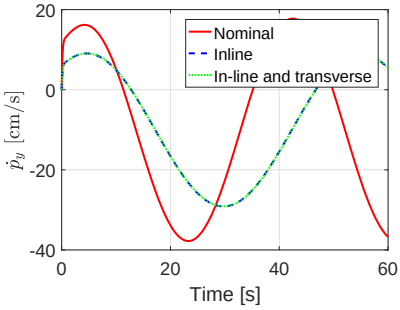

(f) Velocity in y-direction using the actual model

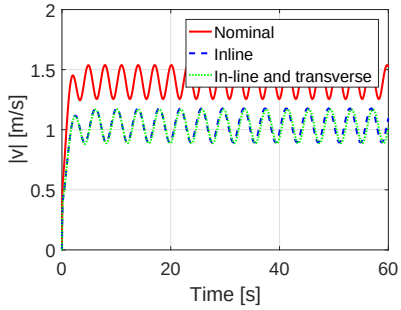

(g) Magnitude of the speed using the small model

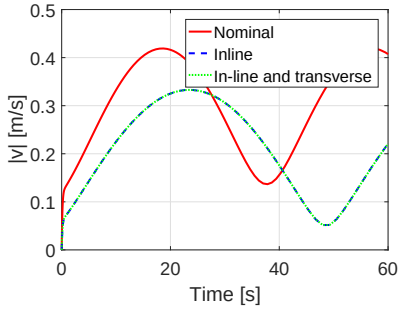

(h) Magnitude of the speed using the actual model

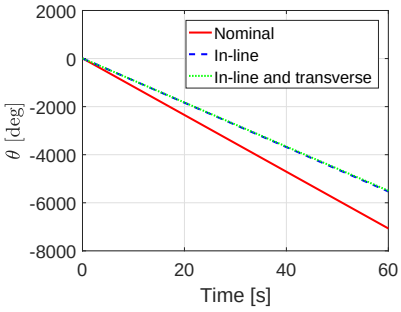

(i) Heading of the robot using the small model

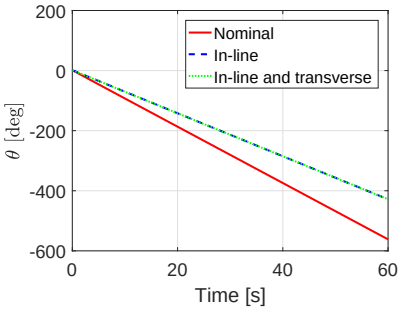

(j) Heading of the robot using the actual model

Figure 5.12: Tests done to study the performance of the underwater snake robot with high speeds in current

5.2 Visual Observations from Full-Scale Tests of Eelume Underwater Snake Robot in a Basin

To study thruster-thruster interactions, thruster-hull interactions, thruster-nearby structure interactions and ventilation, full scale testing is done at Eelume. The pool used to test the underwater snake robot in is shown in figure 5.13. Figure 5.14 shows the underwater snake robot's thrusters. Observations are done for each of the thrust losses to study how they affect the performance of the underwater snake robot. The video from this experiment is attached to the folder delivered with this thesis.

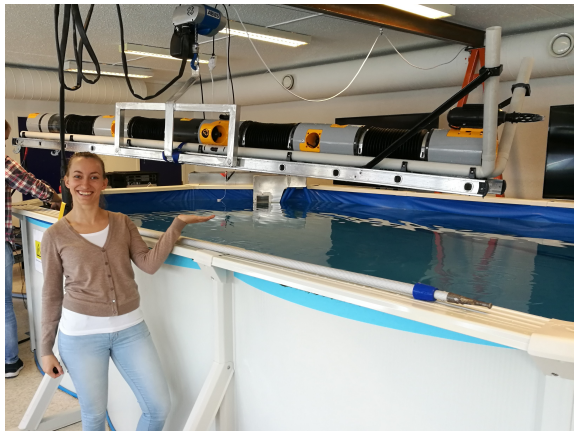

Figure 5.13: Pool with underwater snake robot at Eelume

5.2.1 Thruster-Thruster Interactions

To test the thruster-thruster interactions on the model, the configuration of the underwater snake robot should be formed such that the losses can interfere with the robot's performance. To encourage thruster-thruster interactions, the tunnel thrusters on link two and link four will be positioned as close to each other such that the propeller slip stream from one thruster will reach the other. Hence joint

(a) Tunnel thruster (b) The Underwater Snake Robot with Thrusters (c) Main propeller

Figure 5.14: The configuration of the underwater snake robot with thrusters used in full scale testing at Eelume

number two and three are set to approximately 90°, which is the maximum joint angle.

As seen in the video attached, the thruster-thruster interactions have low effect when the speed is low.

5.2.2 Thruster-Hull Interactions

To encourage the thruster-hull interactions to interfere, it is desirable that the thruster on link three gives a thrust that affects the hull on link two or four. Joint two and three are therefore set to approximately 90°. This is the same position as in Section 5.2.1, thus these tests are done at the same time.

As seen in the video, joint two and three sometimes gets a bigger angle.

5.2.3 Thruster-Nearby Structure Interactions

To encourage thruster-nearby structure interactions, the underwater snake robot is positioned right beside the wall of the pool while the tunnel thrusters use high speed to try and push the underwater snake robot away from the wall. High speed is believed to give a bigger suction.

As seen in the video, the snake robot does not seem to be affected by the wall. The suction mentioned in Section 4.4.5 seems to be negligible.

5.2.4 Ventilation

Ventilation is promoted by placing the underwater snake robot close to the surface and activate the vertical tunnel thrusters. As seen in the video it is clearly present and will give a big impact when the robot is in the presence of the surface.

5.3 Discussion

5.3.1 Simulations in MATLAB

The equations used for K_T and K_Q given in (B.3a) and (B.3b) respectively, are made by quadratic formulas to resemble figure 4.1 as well as possible. To implement accurate values for K_T and K_Q, a propeller open water test need to be done in a towing tank or in a cavitation tunnel. Equations (B.3a) and (B.3b) are only valid for the 1^{st} quadrant, and will need to be changed if the user wants to expand the open water characteristics to a 4-quadrant model with both positive and negative shaft speeds. The ratio P/D is assumed to equal one because of lack of information about the propeller pitch. When executing the simulations in Sections 5.1.1 and 5.1.3, a value of the inflow velocity, $J_a = 0.4$, is assumed. K_T is then found by using J_a

and figure B.2. If the assumed values for J_a, K_T and P/D are wrong, that may have lead to errors in the simulations done in this chapter.

The software code only includes the thrust affected by the thrust losses, and not the torque. To obtain more precised simulations, the torque should also have been included.

The full sized model of the underwater snake robot used by Eelume, is in total 3.4$[m]$ long and weigh 70$[kg]$, where every link is approximately 300$[mm]$ long and weigh approximately 6$[kg]$ in air. The model used in MATLAB are neglecting the size and the weight of the joints, hence 1.9$[m]$ of the length and 40$[kg]$ of the weight of the total model are neglected. This leads to assuming a model that is too small and too light-weighted. Thus the simulation results will not be entirely correct because of less resistance from the model.

All of the simulations are done in 60$[s]$. A longer simulation time could have been chosen to study the underwater snake robot's performance for a longer time span.

Case 1

The underwater snake robot's responses from thrust in its tangential direction are tested in figures 5.1 and 5.2. As seen in both figures, there are no change in the velocity in the y-direction and the heading. This is the behavior expected when no thrust is given in the y-direction. It is also seen that the underwater snake robot's performance with in-line velocity fluctuations is equal to the performance with in-line velocity fluctuations and transverse velocity fluctuations. Since the transverse velocity fluctuations only appear if the thrust has a perpendicular component, there are no such losses in case 1. As seen in figures 5.1c, 5.1d, 5.1g and 5.1h, only the velocity in the x-direction affects the robot and moves it forward in the x-direction as given in figures 5.1a and 5.1b.

When comparing figures 5.1 and 5.2, it is clear that the bigger

the shaft speed is, the bigger the outcome of the underwater snake robot becomes. The size of the robot is also important for how much the robot responds to the thrust given and for how much the robot is affected by the losses. By looking at the figures, it is clear that the small model have bigger movements when applying the same shaft speed as applied to the actual model. The small model also gets greater deflections from the transverse velocity fluctuations. This is because higher shaft speed gives higher thrust, which leads to greater losses.

Case 2

In case 2, the underwater snake robot's responses from thrust given in the normal direction are studied. When the underwater snake robot is formed as a straight line, the CM is placed in the middle of link three. The thrust in this case is applied to link two, which gives the thrust a momentum that will lead to the snake rotating as seen from the paths in figures 5.3a, 5.3b, 5.4a and 5.4b. As shown in figures 5.3 and 5.4, the performance of the robot with in-line velocity fluctuations is equal to the performance of the robot with both in-line velocity fluctuations and transverse velocity fluctuations. This is due to the velocity near the thruster always being in the same direction as the thruster itself. Hence no local transverse component is present.

The global velocity in the x- and y-direction oscillates at the small model with both low and high speed, as shown in figures 5.3c, 5.3e, 5.4c and 5.4e. This is because the snake is turning due to the momentum from the thruster to the CM. Locally the velocity is constant in the y-direction and zero in the x-direction. Figures 5.3g and 5.4g show clearly that the magnitude of the speed is constant.

By comparing the velocities of the real model with low and high speed in figures 5.3d, 5.3f, 5.3h, 5.4d, 5.4f and 5.4h, it is found that there is an obvious difference of the performance with the low and the high speed. With low speed, the velocity in the x-direction is slowly

increasing, while the velocity in the y-direction is slowly decreasing. The reason why it doesn't look like they are oscillating is because actual model is too heavy too move that quickly with only 10[RPS]. If the simulation time had been longer, the oscillations would be present on the graphs.

The heading for both the small model and the actual model in the low speed and high speed cases is constantly decreasing as shown in figures 5.3i, 5.3j, 5.4i and 5.4j. This is as assumed since constant shaft speed is given.

Case 3

In case 3, thrust is given in both the normal direction from link two and in the tangential direction from link three. Figures 5.5a, 5.5b, 5.6a and 5.6b show that this leads to the underwater snake robot to turn while moving forward in its direction. In figures 5.5a, 5.6a and 5.6b it is seen that the path with in-line velocity fluctuations is no longer equal to the path with in-line velocity fluctuations and transverse velocity fluctuations. This is because the velocity near the thrusters is now dependent on two thrusters with different angles of attack. This leads to a transverse component on the thruster on link two because of the influence from the thruster on link three, and a transverse component on the thruster on link three because of the influence from the thruster on link two. This is not seen in figure 5.5b because the actual model is too big compared to the low shaft speed given.

As seen in figures 5.5c, 5.5e, 5.6c, 5.6d, 5.6e and 5.6f the velocity in the x- and y-direction oscillates. It is also seen that the velocity from the in-line velocity fluctuations and transverse velocity fluctuations is delayed compared to in-line velocity fluctuations. The delay is present because the affect from the transverse velocity fluctuations will slow down the underwater snake robot's movements. Both of the losses have the same magnitude in their velocities in the x- and y-

directions. Locally, the magnitude of the velocities with the in-line velocity fluctuations and transverse velocity fluctuations will be lower than the velocities with only in-line velocity fluctuations. Globally, the magnitude will be the same due to the delay. The figures 5.5g, 5.6g and 5.6h show a constant magnitude of speed with no difference between the two losses. This is because as long as the magnitude of the velocities in the x- and y-direction is equal, the sum will also be equal.

When the actual model is affected by the low shaft speed, there is no visible difference between the velocity affected by in-line velocity fluctuations and the velocity affected by in-line velocity fluctuations and transverse velocity fluctuations. This is shown in figures 5.5d, 5.5f and 5.5h. The shaft speed is too slow compared to the size and weight of the model. The size and weight of the model will contribute with increased resistance from the underwater snake robot, which leads to the robot being less affected by the thrust. As shown in figures 5.5g, 5.5h, 5.6g and 5.6h the heading is decreasing constantly as in the previous case. Due to the added thruster in link three the heading decreases faser in this case than the previous case.

Case 4

In case 4, a thruster is added on link three with an angle of 15°. This thruster does not exist on the underwater snake robot studied in this thesis, but the author wanted to study what effects it would have had. Figures 5.7a, 5.7b, 5.8a and 5.8b show that the robot moves forward while it turns, which is the path expected. The difference between the velocity given in the x- and y-direction with in-line velocity fluctuations and the velocity given in the x- and y-direction with in-line velocity fluctuations and transverse velocity fluctuations is to small to be visible on figures 5.7c, 5.7d, 5.7e, 5.7f, 5.7g, 5.7h, 5.8d, 5.8f and 5.8h. In the case of the small model with the high speed, the results

are different. As shown in figures 5.8c, 5.8e and 5.8g, the delay of the in-line velocity fluctuations and transverse velocity fluctuations are present. Thus the smaller the model, and the larger the shaft speed, the larger the differences become between the two losses. It is also assumed that the greater the angle of attack becomes, the larger the differences become. The heading is, as expected, constantly decreasing as seen in figures 5.7i, 5.7j, 5.8i and 5.8j.

The Influence of K_T

The influence of the value of K_T is studied in figures 5.9 and 5.10. The larger J_a is, the smaller K_T becomes. As seen in the figures, a smaller K_T gives less performance in both velocity and heading which leads to a shorter and less accurate path. The differences are bigger in the small model than in the actual model, and they get bigger with higher shaft speed. Hence, the larger K_T, the smaller model and the higher speed, give the largest influence.

Adding Current

The model proposed in Kelasidi et al. (2017) takes into account the current effects. Based on this model, simulation results for thrust losses under the influence of ocean currents are obtained in this thesis. Current is already implemented in the software code used in Kelasidi et al. (2017). When adding the current to the code added in this thesis, the underwater snake robot's reaction to current can be studied. The tunnel thruster on link two is activated during the tests. By using the low shaft speed, both the small model and the actual model moves approximately in a straight line as seen in figures 5.11a and 5.11b. By using the high shaft speed, both the small model and the actual model moves in the same direction as before and oscillates in circles at the same time as shown in figures 5.12a and 5.12b.

The influence of the current is clearly shown by comparing figures 5.11 and 5.12 with 5.3 and 5.4 since both cases gives the same thrust. It is seen that the current affects the performance of the underwater snake robot. The positive current given in the x-direction increases the global velocity in the x-direction, while the negative current given in the y-direction decreases the global velocity in the y-direction. It can also be seen that the magnitude of the velocity with current oscillates around a higher speed than in the case with no current, as seen in figures 5.11g and 5.3g respectively. By applying high speed to the small model, the velocities oscillates with a higher frequency as shown in figures 5.12c, 5.12e and 5.12g. Compared to figures 5.3c, 5.3e and 5.3g, the velocity in the x-direction gets higher by adding current, while the velocity in the y-direction becomes lower by adding current. This is because of the direction of the current added. The magnitude of velocity is constant without current, while it oscillates when current is added. This is due to the rotation of the robot.

By studying the performance of the actual model, it is given that the velocity in the x-direction have increased by adding current and that the velocity in the y-direction have decreased by adding current, as given in figures 5.11d and 5.11f respectively. The magnitude of the speed has increased in figure 5.12h compared to figure 5.3h. This is because the low speed is too low to make a great impact on the actual model, while by adding the current, the model gets the push it needs to move the distance. There is no oscillations when adding $10[RPS]$, while when adding $63[RPS]$, oscillations are present. The oscillations are shown in figures 5.12d, 5.12f and 5.12h. By comparison with figures 5.4d, 5.4f and 5.4h, it is shown that the x-velocity increases by adding current and that the y-velocity decreases by adding current.

In all of the figures for the underwater snake robot with current it is found that the the cases with in-line velocity fluctuations and the cases with in-line velocity fluctuations and transverse velocity fluctuations

are approximately equal. The exception is for the small model with high velocities, where there is a small difference between the two losses. It is believed that with higher angle of attack there would have been a more defined difference between the losses from the in-line velocity fluctuations and the losses from the in-line velocity fluctuations and transverse velocity fluctuations. The heading in figures 5.11i, 5.11j, 5.12i and 5.12j is decreasing constantly because of the constant thrust added.

5.3.2 Full Scale Testing

When testing the thruster-thruster interactions, the expected consequence is for the inflow velocity to the affected thruster to be changed by the propeller slip stream from the source thruster. This is not visible in the video attached. It is believed that the velocity from the wake from the source thruster has decreased so much when it reaches the affected thruster, that it is negligible. This is due to the large distance between the two links with the tunnel thrusters. The larger the distance is, the more the wake from the source thruster will decrease. As long as the underwater snake robot do not have tunnel thrusters on neighboring links, the length of the links doesn't change and the joints can't bend more than 90°, the thruster-thruster interactions will not be of significance on the underwater snake robot. With higher velocity the thrust loss may give a bigger effect.

The thruster-hull interactions are encouraged by trying to activate the thrust given from the main propellers to interfere with the neighboring links. It is expected that the second or third joint's angle will increase. As shown in the video, this happens. This can both be because of the thruster-hull interactions and because of the drag. Drag affects the snake in a large amount, and can therefore be assumed to be the main reason for this movement. Due to the snake robot's slender body, the Coanda effect is assumed to be negligible.

The thruster-nearby structure interactions are negligible as shown in the video. Even at 2[min] in the video, where the tunnel thruster is as close to the wall as possible, no suction is present to the naked eye. Suction is probably there, but the observations show that it is not big enough to give a great impact on underwater snake robot. By using a smaller model or higher speed the suction may have been visible.

According to the observations, ventilation is present when the underwater snake robot is near the surface. The funnels mentioned in Section 4.4.6 are visible and the thruster is attracting a lot of air. This may lead to wear and tear. The funnels are only visible when the robot is at the surface, and not when it is deeply submerged. Thus it is assumed that this loss will not be of big importance since the underwater snake robot operates at deeply submerged water. Since this is only an observation and no thrust losses are measured in any way, it is not known for sure how this phenomenon affects the overall motion of the robot.

5.3.3 Control System

The control system given in figure 4.5 is a rough overview of how the final control system may look like. The results from the simulations show that the thrust losses leads to a weaker performance than the desired (nominal) one. This problem is solved in the controller in the control system. The controller will receive the actual thrust, and compare this to the desired one. An error, $e = T_d - T_a$, will be made and the controller will use an algorithm to minimize the error. Hence the controller will make up for the thrust losses affecting the underwater snake robot.

The control system should also account for forbidden sectors. Forbidden sectors are sectors where the underwater snake robot is in an unfortunate position. It can be that the thruster-thruster interactions or the thruster-hull interactions are causing thrust losses or that the

underwater snake robot is too close to another structure. When passing through forbidden sectors the thrusters are allowed to produce thrust, but they will pass the forbidden sectors as fast as possible as explained in Ruth (2008). While passing forbidden sectors, the underwater snake robot can be commanded to reduce its thrust magnitude. This will reduce the magnitude of the thrust losses.

Chapter 6

Concluding Remarks

6.1 Conclusions

The aim of this thesis was to study thrust losses that affect the underwater snake robot while moving with constant positive shaft speeds. Two of the thrust losses, in-line velocity fluctuations and transverse velocity fluctuations, were studied by simulating several cases in MATLAB. The simulations showed that the software code works well due to expected results. The smaller the model was and the larger the shaft speeds were, the bigger the thrust losses became. Since Eelume's underwater snake robot is primary used in operations done in station keeping, these thrust losses will be small. When the robot moves in transit, the in-line velocity fluctuations will give a greater impact than the transverse velocity fluctuations.

The K_T value in the open water characteristics had a big influence on the performance of the underwater snake robot. Smaller K_T-value gave greater thrust losses. When current was added to the software code, the underwater snake robot responded to the current as expected.

The last four of the thrust losses, thruster-thruster interactions, thruster-hull interactions, thruster-nearby structure interactions and

ventilation, were studied by full scale testing at Eelume. These tests showed that as long as the thrusters were positioned the way they are now and the joints couldn't bend more than 90°, the impacts from thruster-thruster interactions, thruster-hull interactions and thruster-nearby structure interactions seemed to be negligible. Thrust losses from ventilation seemed to be present when the underwater snake robot was near the surface of the water.

6.2 Further Work

Exact values for K_T and K_Q should be determined in further work. This can be done by propeller open water tests in either a cavitation tunnel or a towing tank. An accurate relationship between the constants K_T/K_Q and J_a will be obtained. The open water characteristics in figure B.2 could also be expanded to a 4-quadrant model to include negative shaft speeds as well. Adding a precise propeller open water characteristics and including negative shaft speeds, will ensure the future simulations to be more accurate.

The torque should also be included in the model. So far it is assumed to be zero. Using (4.1b) and K_Q found by the open water tests, the exact torque can be found.

To improve the simulations further, thruster-thruster interactions, thurster-hull interactions, thruster-nearby structure interactions and ventilation should be implemented in the software code even though they are small. It is recommended to do tests in a lab to develop and employ mathematical models for these thrust losses. Using the tests, verification of thrust loss models could be done.

A control system should be applied. The controller in the control system will make up for the error between the desired and the actual thrust. Hence the controller will add more thrust until the actual thrust becomes equal to the desired thrust. A shaft speed controller

works well for slow speeds. Since the snake robot will act mostly in station keeping, a shaft speed controller would probably work best.

Forbidden sectors should also be implemented in the control system to prevent the robot of getting in unfortunate positions. Finally, inputs for the $\boldsymbol{K}_{tr}$-matrix in the thruster allocation should be included. When all of the mentioned improvements are done, different configurations of the thrusters can be tested to see if any other configuration works better.

Bibliography

Blanke, M. (1981). *Ship propulsion losses related to automatic steering and prime mover control.* Phd thesis, Servolaboratory, Technical University of Denmark.

Blanke, M., Fossen, T. I., and Lindegaard, K.-P. (2000). Dynamic model for thrust generation of marine propellers. *IFAC Manoeuvring and Control of Marine Craft*, pages 363–368.

BlueRobotics (2017a). T200 Thruster. `https://www.bluerobotics.com/store/thrusters/t200-thruster/`.

BlueRobotics (2017b). T200 Thruster Documentation. `http://docs.bluerobotics.com/thrusters/t200/#introduction`.

Carlton, J. S. (2007). *Marine Propellers and Propulsion.* Elsevier, Amsterdam, 2nd edition.

Eelume (2017). Eelume - Subsea Intervention. `https://eelume.com/`.

Faltinsen, O. M. (1990). *Sea Loads on Ships and Offshore Structures.* Cambridge Ocean Technology Series. Cambridge University Press, Cambridge.

Faltinsen, O. M. (2005). *Hydrodynamics of High-Speed Marine Vehicles.* Cambridge University Press, Cambridge.

Fossen, T. I. (2011). *Handbook of Marine Craft Hydrodynamics and Motion Control.* Wiley, Chichester.

Fossen, T. I. and Blanke, M. (2000). Nonlinear output feedback control of underwater vehicle propellers using feedback form estimated axial flow velocity. *IEEE Journal of Oceanic Engineering*, 25(2):241–255.

Galta, M. (2017). Thrust losses on underwater swimming manipulators. Pre project thesis, Department of Marine Technology, Faculty of Engineering Science & Technology, Norwegian University of Science and Technology.

Hirose, S. and Yamada, H. (2009). Snake-like robots. *IEEE Robotics & Automation Magazine*, 16(1):88–98.

Kelasidi, E. (2015). *Modeling, Control and Energy Efficiency of Underwater Snake Robots*. Phd thesis, Department of Engineering Cybernetics, Faculty of Information Technology, Mathematics & Electrical Engineering, Norwegian University of Science and Technology.

Kelasidi, E., Pettersen, K. Y., and Gravdahl, J. T. (2014a). Modeling of underwater snake robots moving in a vertical plane in 3d. *IEEE/RSJ International Conference on Intelligent Robots and Systems*, pages 266 – 273.

Kelasidi, E., Pettersen, K. Y., and Gravdahl, J. T. (2015). Energy efficiency of underwater robots. *IFAC-PapersOnLine*, 48(16):152–159.

Kelasidi, E., Pettersen, K. Y., Gravdahl, J. T., and Liljebäck, P. (2014b). Modeling of underwater snake robots. *IEEE International Conference on Robotics and Automation (ICRA)*, pages 4540–4547.

Kelasidi, E., Pettersen, K. Y., Gravdahl, J. T., Strømsøyen, S., and Sørensen, A. J. (2017). Modeling and propulsion methods of underwater snake robots. *IEEE Conference on Control Technology and Applications*.

Kelasidi, E., Pettersen, K. Y., Liljebäck, P., and Gravdahl, J. T. (2014c). Integral line-of-sight for path-following of underwater snake robots. *IEEE Multi-Conference on Systems and Control*, pages 1078–1085.

Lehn, E. (1992). *Practical Methods for Estimation of Thrust Losses*, volume 513003.00.06 of *Marintek rapport (trykt utg.)*. Norwegian Marine Technology Research Institute, Trondheim.

Liljebäck, P., Pettersen, K. Y., and Stavdahl, Ø. (2010). A snake robot with a contact force measurement system for obstacle-aided locomotion. *IEEE International Conference on Robotics and Automation (ICRA 2010)*, pages 683–690.

Liljebäck, P., Pettersen, K. Y., and Stavdahl, Ø. (2012a). *Snake Robots: Modelling, Mechatronics, and Control*. Snake Robots: Modelling, Mechatronics, and Control. Springer, Dordrecht.

Liljebäck, P., Pettersen, K. Y., Stavdahl, Ø., and Gravdahl, J. T. (2012b). A review on modelling, implementation, and control of snake robots. *Robotics and Autonomous Systems*, 60(1):29–40.

Liljebäck, P., Stavdahl, Ø., Pettersen, K. Y., and Gravdahl, J. (2014). Mamba – a waterproof snake robot with tactile sensing. *IEEE/RSJ International Conference on Intelligent Robots and Systems*, pages 294 – 301.

Maritime, K. (2017). ROBOTIC 'SNAKE' VIDEO RELEASED. `http://stories.kongsberg.com/content/robotic-snake-video-released`.

Molland, A. F., Turnock, S. R., and Hudson, D. A. (2011). *Ship Resistance and Propulsion: Practical Estimation of Ship Propulsive Power*. Ship Resistance & Propulsion. Cambridge University Press, Cambridge.

Nysgjerrigper (2017). Slangerobot er Vaktmeister i Djupet. https://nysgjerrigper.no/Artikler/2017/januar/robotslangen.

ROBO-NEWS (2017). SUNKEN TREASURE SHIP DISCOVERED BY SUBSEA ROV. http://roboglobal.com/sunken-treasure-ship-discovered-by-subsea-rov.

Robotics and Systems, E. (2017). Research Report of Snake-like Robot. http://www6.in.tum.de/pub/Main/WebHome/sanke_robot_intro.pdf.

ROBOTNOR (2017a). Anna Konda – The Fire Fighting Snake Robot. http://robotnor.no/research/anna-konda-the-fire-fighting-snake-robot/.

ROBOTNOR (2017b). Kulko - A Snake Robot with Tactile Sensors. http://robotnor.no/research/kulko-a-snake-robot-with-tactile-sensors/.

ROBOTNOR (2017c). Mamba - Our New Modular Snake Robot. http://robotnor.no/research/mamba-our-new-modular-snake-robot/.

ROBOTNOR (2017d). Wheeko - A Snake Robot with Passive Wheels. http://robotnor.no/research/wheeko-a-snake-robot-with-passive-wheels/.

Ruth, E. (2008). *Propulsion Control and Thrust Allocation on Marine Vessels*. Phd thesis, Department of Marine Technology, Faculty of Engineering Science & Technology, Norwegian University of Science and Technology.

Schlichting, H. (1979). *Boundary-Layer Theory*. Grenzschicht-Theorie. McGraw-Hill, New York, 7th edition.

SINTEF (2017a). Anna Konda – The Fire Fighting Snake Robot. https://www.sintef.no/en/information-and-communication-technology-ict/departments/applied-cybernetics/projects/our-snake-robots/anna-konda--the-fire-fighting-snake-robot/.

SINTEF (2017b). SnakeFighter. https://www.sintef.no/en/information-and-communication-technology-ict/departments/applied-cybernetics/projects/snakefighter/.

Smogeli, Ø. N. (2006). *Control of Marine Propellers - From Normal to Extreme Conditions*. Phd thesis, Department of Marine Technology, Faculty of Engineering Science & Technology, Norwegian University of Science and Technology.

Sørensen, A. J. (2013). *Marine Control Systems: Propulsion and Motion Control of Ships and Ocean Structures*, volume UK-2013-76 of *Compendium (Norwegian University of Science and Technology, Department of Marine Technology)*. Norwegian University of Science and Technology, Department of Marine Technology, Trondheim.

Steen, S. (2014). *TMR4220 Naval Hydrodynamics Foil and Propeller Theory: Lecture Notes*, volume UK-2014-80/II of *Compendium (Norwegian University of Science and Technology, Department of Marine Technology)*. Norwegian University of Science and Technology, Department of Marine Technology, Trondheim.

Strømsøyen, S. (2015). Propulsion methods for under water snake robots: Investigation and simulation using foil for propulsion of a snake robot. Msc thesis, Department of Marine Technology, Faculty of Engineering Science & Technology, Norwegian University of Science and Technology.

Sverdrup-Thygeson, J., Kelasidi, E., Pettersen, K. Y., and Gravdahl, J. T. (2016a). A control framework for biologically inspired un-

derwater swimming manipulators equipped with thrusters. *IFAC-PapersOnLine*, 49(23):89–96.

Sverdrup-Thygeson, J., Kelasidi, E., Pettersen, K. Y., and Gravdahl, J. T. (2016b). Modeling of underwater swimming manipulators. *IFAC-PapersOnLine*, 49(23):81–88.

Technology, U. S. (2017). Bluefin SandShark Micro-AUVs Successfully Launched From AUV. `http://www.unmannedsystemstechnology.com/2016/09/general-dynamics-launches-bluefin-sandshark-micro-auvs-during-u-s-navy-exercise/`.

Transeth, A. A. (2007). *Modelling and Control of Snake Robots*. Phd thesis, Department of Engineering Cybernetics, Faculty of Information Technology, Mathematics & Electrical Engineering, Norwegian University of Science and Technology.

Trendhunter (2017). Serpentine Industrial Robots. `https://www.trendhunter.com/trends/euleme-snake-robot`.

Appendix A

Basic Notation

$$\boldsymbol{A} = \begin{bmatrix} 1 & 1 & & & \\ & . & . & & \\ & & . & . & \\ & & & . & . \\ & & & 1 & 1 \end{bmatrix} \in \mathbb{R}^{(N-1)\times N} \tag{A.1}$$

$$\boldsymbol{D} = \begin{bmatrix} 1 & -1 & & & \\ & . & . & & \\ & & . & . & \\ & & & . & . \\ & & & 1 & -1 \end{bmatrix} \in \mathbb{R}^{(N-1)\times N} \tag{A.2}$$

$$\boldsymbol{e} = \begin{bmatrix} 1, & ..., & 1 \end{bmatrix}^T \in \mathbb{R}^N \tag{A.3}$$

$$\boldsymbol{E} = \begin{bmatrix} \boldsymbol{e} & \boldsymbol{0}_{N\times 1} \\ \boldsymbol{0}_{N\times 1} & \boldsymbol{e} \end{bmatrix} \in \mathbb{R}^{2N\times 2} \tag{A.4}$$

$$sin(\boldsymbol{\theta}) = \begin{bmatrix} sin(\theta_1), & ..., & sin(\theta_N) \end{bmatrix}^T \in \mathbb{R}^N \tag{A.5}$$

$$\boldsymbol{S_\theta} = diag(sin\boldsymbol{\theta}) \in \mathbb{R}^{N\times N} \tag{A.6}$$

$$cos(\boldsymbol{\theta}) = \Big[cos(\theta_1), \quad ..., \quad cos(\theta_N)\Big]^T \in \mathbb{R}^N \tag{A.7}$$

$$\boldsymbol{C_\theta} = diag(cos\boldsymbol{\theta}) \in \mathbb{R}^{N\times N} \tag{A.8}$$

$$sgn(\boldsymbol{\theta}) = \Big[sgn(\theta_1), \quad ..., \quad sgn(\theta_N)\Big]^T \in \mathbb{R}^N \tag{A.9}$$

$$\boldsymbol{\dot\theta^2} = \Big[\dot\theta_1^2, \quad ..., \quad \dot\theta_N^2\Big]^T \in \mathbb{R}^N \tag{A.10}$$

$$\boldsymbol{M} = diag([m_1, ..., m_N]) \in \mathbb{R}^{N\times N} \tag{A.11}$$

$$\boldsymbol{L} = diag([l_1, ..., l_N]) \in \mathbb{R}^{N\times N} \tag{A.12}$$

$$\boldsymbol{J} = diag([j_1, ..., j_N]) \in \mathbb{R}^{N\times N} \tag{A.13}$$

$$\boldsymbol{K} = \boldsymbol{L}\boldsymbol{A}^T(\boldsymbol{D}\boldsymbol{M}^{-1}\boldsymbol{D}^T)^{-1}\boldsymbol{D}\boldsymbol{M}^{-1} \tag{A.14}$$

$$\boldsymbol{V} = \boldsymbol{L}\boldsymbol{A}^T(\boldsymbol{D}\boldsymbol{D}^T)^{-1}\boldsymbol{D} \tag{A.15}$$

$$\boldsymbol{V_1} = \boldsymbol{V}\boldsymbol{M}\boldsymbol{K}^T \tag{A.16}$$

$$\boldsymbol{V_2} = \boldsymbol{V}\boldsymbol{M}\boldsymbol{e} \tag{A.17}$$

$$\boldsymbol{M_p} = \begin{bmatrix} m_{11} & m_{12} \\ m_{21} & m_{22} \end{bmatrix} = \begin{bmatrix} m_t + \boldsymbol{e}^T{\boldsymbol{S_\theta}}^2\boldsymbol{\mu}\boldsymbol{e} & -\boldsymbol{e}^T\boldsymbol{S_\theta}\boldsymbol{C_\theta}\boldsymbol{\mu}\boldsymbol{e} \\ -\boldsymbol{e}^T\boldsymbol{S_\theta}\boldsymbol{C_\theta}\boldsymbol{\mu}\boldsymbol{e} & m_t + \boldsymbol{e}^T{\boldsymbol{C_\theta}}^2\boldsymbol{\mu}\boldsymbol{e} \end{bmatrix}^{-1} \tag{A.18}$$

$$\boldsymbol{N_p} = \begin{bmatrix} \boldsymbol{e}^T \boldsymbol{S_\theta} \boldsymbol{C_\theta} \boldsymbol{\mu} & \boldsymbol{e}^T \boldsymbol{S_\theta}^2 \boldsymbol{\mu} \\ -\boldsymbol{e}^T \boldsymbol{C_\theta}^2 \boldsymbol{\mu} & -\boldsymbol{e}^T \boldsymbol{S_\theta} \boldsymbol{C_\theta} \boldsymbol{\mu} \end{bmatrix} \tag{A.19}$$

$$\boldsymbol{L_p} = \begin{bmatrix} \boldsymbol{e}^T \boldsymbol{S_\theta}^2 \boldsymbol{\mu} & -\boldsymbol{e}^T \boldsymbol{S_\theta} \boldsymbol{C_\theta} \boldsymbol{\mu} \\ -\boldsymbol{e}^T \boldsymbol{S_\theta} \boldsymbol{C_\theta} \boldsymbol{\mu} & \boldsymbol{e}^T \boldsymbol{C_\theta}^2 \boldsymbol{\mu} \end{bmatrix} \tag{A.20}$$

$$\begin{aligned} \boldsymbol{M_\theta} = \boldsymbol{J} + \boldsymbol{S_\theta} \boldsymbol{V_1} \boldsymbol{S_\theta} + \boldsymbol{C_\theta} \boldsymbol{V_1} \boldsymbol{C_\theta} - \boldsymbol{S_\theta} \boldsymbol{V} \boldsymbol{A_1} + \boldsymbol{C_\theta} \boldsymbol{V} \boldsymbol{A_4} \\ + \boldsymbol{K_5} \boldsymbol{K_1} \boldsymbol{K}^T \boldsymbol{S_\theta} - \boldsymbol{K_5} \boldsymbol{K_2} \boldsymbol{K}^T \boldsymbol{C_\theta} + \boldsymbol{K_6} \boldsymbol{K_4} \boldsymbol{K}^T \boldsymbol{C_\theta} + \Lambda_1 \end{aligned} \tag{A.21}$$

$$\begin{aligned} \boldsymbol{W_\theta} = +\boldsymbol{S_\theta} \boldsymbol{V_1} \boldsymbol{C_\theta} - \boldsymbol{C_\theta} \boldsymbol{V_1} \boldsymbol{S_\theta} - \boldsymbol{S_\theta} \boldsymbol{V} \boldsymbol{A_2} + \boldsymbol{C_\theta} \boldsymbol{V} \boldsymbol{A_5} + \boldsymbol{K_5} \boldsymbol{K_1} \boldsymbol{K}^T \boldsymbol{C_\theta} \\ + \boldsymbol{K_5} \boldsymbol{K_2} \boldsymbol{K}^T \boldsymbol{S_\theta} + \boldsymbol{K_6} \boldsymbol{K_3} \boldsymbol{K}^T \boldsymbol{C_\theta} - \boldsymbol{K_6} \boldsymbol{K_4} \boldsymbol{K}^T \boldsymbol{S_\theta} \end{aligned} \tag{A.22}$$

$$\begin{aligned} \boldsymbol{V_{\theta,\dot{\theta}}} = -\boldsymbol{S_\theta} \boldsymbol{V} diag(\dot{\boldsymbol{\theta}}) \boldsymbol{A_3} + \boldsymbol{C_\theta} \boldsymbol{V} diag(\dot{\boldsymbol{\theta}}) \boldsymbol{A_6} - \boldsymbol{K_5} \boldsymbol{K_2} diag(\dot{\boldsymbol{\theta}}) \boldsymbol{K}^T \boldsymbol{S_\theta} \\ - \boldsymbol{K_5} \boldsymbol{K_1} diag(\dot{\boldsymbol{\theta}}) \boldsymbol{K}^T \boldsymbol{C_\theta} + \boldsymbol{K_6} \boldsymbol{K_4} diag(\dot{\boldsymbol{\theta}}) \boldsymbol{K}^T \boldsymbol{S_\theta} \\ - \boldsymbol{K_6} \boldsymbol{K_3} diag(\dot{\boldsymbol{\theta}}) \boldsymbol{K}^T \boldsymbol{C_\theta} + \Lambda_2 + \Lambda_3 diag(|\dot{\boldsymbol{\theta}}|) \end{aligned} \tag{A.23}$$

$$\boldsymbol{N_{\theta,\dot{\theta}}} = (\boldsymbol{S_\theta} \boldsymbol{V} \boldsymbol{S_\theta} \boldsymbol{C_\theta} \boldsymbol{\mu} + \boldsymbol{C_\theta} \boldsymbol{V} \boldsymbol{C_\theta}^2 \boldsymbol{\mu} - \boldsymbol{K_5} \boldsymbol{K_2} + \boldsymbol{K_6} \boldsymbol{K_4}) diag(\dot{\boldsymbol{\theta}}) \tag{A.24}$$

$$\boldsymbol{P_{\theta,\dot{\theta}}} = (\boldsymbol{S_\theta} \boldsymbol{V} \boldsymbol{S_\theta}^2 \boldsymbol{\mu} + \boldsymbol{C_\theta} \boldsymbol{V} \boldsymbol{S_\theta} \boldsymbol{C_\theta} \boldsymbol{\mu} + \boldsymbol{K_5} \boldsymbol{K_1} + \boldsymbol{K_6} \boldsymbol{K_3}) diag(\dot{\boldsymbol{\theta}}) \tag{A.25}$$

$$\boldsymbol{K_x} = -\boldsymbol{S_\theta} \boldsymbol{V} - \boldsymbol{K_5} m_{11} \boldsymbol{e}^T - \boldsymbol{K_6} m_{21} \boldsymbol{e}^T \tag{A.26}$$

$$\boldsymbol{K_y} = \boldsymbol{C_\theta} \boldsymbol{V} - \boldsymbol{K_5} m_{12} \boldsymbol{e}^T - \boldsymbol{K_6} m_{22} \boldsymbol{e}^T \tag{A.27}$$

$$\boldsymbol{A_1} = -\boldsymbol{S_\theta}^2 \boldsymbol{\mu} \boldsymbol{K}^T \boldsymbol{S_\theta} - \boldsymbol{S_\theta} \boldsymbol{C_\theta} \boldsymbol{\mu} \boldsymbol{K}^T \boldsymbol{C_\theta} \tag{A.28}$$

$$\boldsymbol{A_2} = -\boldsymbol{S_\theta}^2\boldsymbol{\mu}\boldsymbol{K}^T\boldsymbol{C_\theta} + \boldsymbol{S_\theta}\boldsymbol{C_\theta}\boldsymbol{\mu}\boldsymbol{K}^T\boldsymbol{S_\theta} \tag{A.29}$$

$$\boldsymbol{A_3} = -\boldsymbol{S_\theta}\boldsymbol{C_\theta}\boldsymbol{\mu}\boldsymbol{K}^T\boldsymbol{S_\theta} + \boldsymbol{S_\theta}^2\boldsymbol{\mu}\boldsymbol{K}^T\boldsymbol{C_\theta} \tag{A.30}$$

$$\boldsymbol{A_4} = \boldsymbol{S_\theta}\boldsymbol{C_\theta}\boldsymbol{\mu}\boldsymbol{K}^T\boldsymbol{S_\theta} + \boldsymbol{C_\theta}^2\boldsymbol{\mu}\boldsymbol{K}^T\boldsymbol{C_\theta} \tag{A.31}$$

$$\boldsymbol{A_5} = \boldsymbol{S_\theta}\boldsymbol{C_\theta}\boldsymbol{\mu}\boldsymbol{K}^T\boldsymbol{C_\theta} - \boldsymbol{C_\theta}^2\boldsymbol{\mu}\boldsymbol{K}^T\boldsymbol{S_\theta} \tag{A.32}$$

$$\boldsymbol{A_6} = \boldsymbol{C_\theta}^2\boldsymbol{\mu}\boldsymbol{K}^T\boldsymbol{S_\theta} - \boldsymbol{S_\theta}\boldsymbol{C_\theta}\boldsymbol{\mu}\boldsymbol{K}^T\boldsymbol{C_\theta} \tag{A.33}$$

$$\boldsymbol{K_1} = m_{11}\boldsymbol{e}^T\boldsymbol{S_\theta}^2\boldsymbol{\mu} - m_{12}\boldsymbol{e}^T\boldsymbol{S_\theta}\boldsymbol{C_\theta}\boldsymbol{\mu} \tag{A.34}$$

$$\boldsymbol{K_2} = -m_{11}\boldsymbol{e}^T\boldsymbol{S_\theta}\boldsymbol{C_\theta}\boldsymbol{\mu} + m_{12}\boldsymbol{e}^T\boldsymbol{C_\theta}^2\boldsymbol{\mu} \tag{A.35}$$

$$\boldsymbol{K_3} = m_{21}\boldsymbol{e}^T\boldsymbol{S_\theta}^2\boldsymbol{\mu} - m_{22}\boldsymbol{e}^T\boldsymbol{S_\theta}\boldsymbol{C_\theta}\boldsymbol{\mu} \tag{A.36}$$

$$\boldsymbol{K_4} = m_{21}\boldsymbol{e}^T\boldsymbol{S_\theta}\boldsymbol{C_\theta}\boldsymbol{\mu} - m_{22}\boldsymbol{e}^T\boldsymbol{C_\theta}^2\boldsymbol{\mu} \tag{A.37}$$

$$\boldsymbol{K_5} = -\boldsymbol{S_\theta}\boldsymbol{V_2} - \boldsymbol{S_\theta}\boldsymbol{V}\boldsymbol{S_\theta}^2\boldsymbol{\mu}\boldsymbol{e} - \boldsymbol{C_\theta}\boldsymbol{V}\boldsymbol{S_\theta}\boldsymbol{C_\theta}\boldsymbol{\mu}\boldsymbol{e} \tag{A.38}$$

$$\boldsymbol{K_6} = \boldsymbol{C_\theta}\boldsymbol{V_2} + \boldsymbol{S_\theta}\boldsymbol{V}\boldsymbol{S_\theta}\boldsymbol{C_\theta}\boldsymbol{\mu}\boldsymbol{e} + \boldsymbol{C_\theta}\boldsymbol{V}\boldsymbol{C_\theta}^2\boldsymbol{\mu}\boldsymbol{e} \tag{A.39}$$

Appendix B

Input Data

The underwater snake robot used in this chapter has five links and four joints. Two main propellers which are used for forward velocity are added in link number three, while tunnel thrusters are added in link two and four to help with sideways and vertical movement. Since this thesis is restricted for the underwater snake robot to move in the horizontal 2D space, the vertical tunnel thrusters are neglected.

The model used in the simulations in MATLAB is given in figure B.1. In the figure, the placements of the links are shown, and the local and global coordinate systems are given. Between each of the links, the joints are placed. The angular deflection of the joints is 90° at the maximum.

The software code used for the simulations in MATLAB consists of several scripts working together. The script added by the author calculates the values for f_{tx} and f_{ty} and include them in (3.22). This script is shown in Appendix C.

The user needs to give two inputs to the code: the shaft speed at each thruster and the angle of attack for each thruster. Shaft speed is given as shown in (B.1) where the shaft speed for the thruster at link one is given in column one, shaft speed of link two is given in column two and so on. If there are no thrusters on the link, the RPS will be

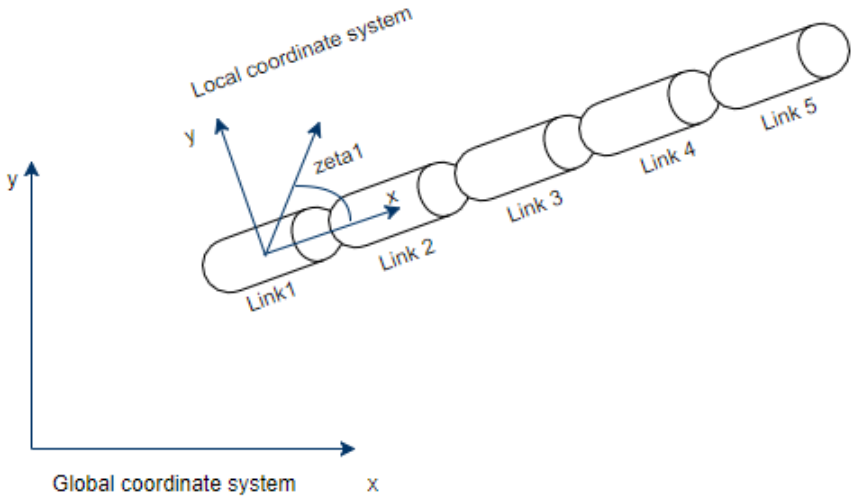

Figure B.1: The model of the Underwater Snake Robot with thrusters used in MATLAB

zero.

$$RPS = \begin{bmatrix} RPS_1 & RPS_2 & ... & RPS_N \end{bmatrix} \tag{B.1}$$

The vector for the angles of attack is shown in (B.2) where the angle of attack for the thruster on the first link is given in the first column and so on. The angle of attack is given in local coordinates and is shown in figure B.1. The ζ-values are given in radians.

$$zeta = \begin{bmatrix} zeta_1 & zeta_2 & ... & zeta_N \end{bmatrix} \tag{B.2}$$

In the model of the forces from the added effectors given in Section 3.3, the number of thrusters, k, is a scalar from one to N. This means that the model used in this thesis can have maximum one thruster for each link. To add more thrusters, either a new model has to be made, or the angle of attack and magnitude of the shaft speed has to be calculated by the user before implementing the values.

B.1 In-Line Velocity Fluctuations

Equations (4.1a) and (4.1b) are used to calculate the thrust and torque due to the losses from in-line velocity fluctuations. Parameters needed to calculate the thrust and torque are K_T, K_Q, ρ, D and n. The parameters ρ and D are constants, n is set by the user and K_T and K_Q can vary by time. The coefficients K_T and K_Q are found by using the open water characteristics as in figure 4.1. The constants are dependent on J_a, which is given in (4.4). It is assumed that K_T and K_Q can be calculated by (B.3a) and (B.3b), which are second degree equations that are inspired by the open water characteristics found in Sørensen (2013) where $P/D = 1$. The open water characteristics found by using (B.3a) and (B.3b) are shown in figure B.2.

$$K_{T,i} = -0.15J_{a,i}^2 - 0.25J_{a,i} + 0.4 \tag{B.3a}$$

$$K_{Q,i} \cdot 10 = -0.2J_{a,i}^2 - 0.3J_{a,i} + 0.6 \tag{B.3b}$$

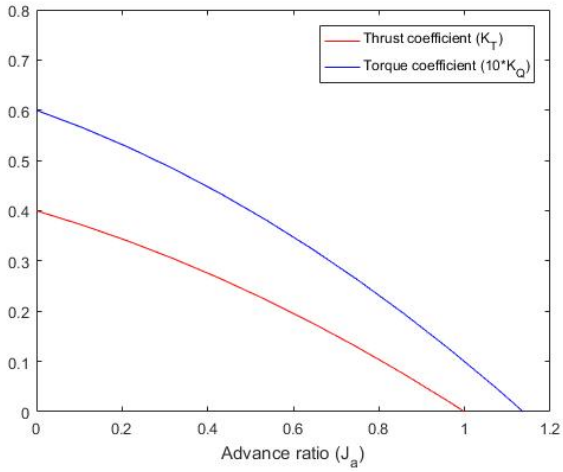

Figure B.2: Propeller open water characteristics used in the simulations in this thesis

The torque is assumed to equal zero, thus K_Q is not used in this thesis

B.2 Transverse Velocity Fluctuations

The equations used to calculate the transverse velocity fluctuations are (4.11) and (4.12). The parameters needed for these equations are ρ, K_{cc}, D, V_{tr} and T_{il}. The coefficient $K_{cc} = 0.25$ is a given constant for ducted propellers found in Sørensen (2013) and Lehn (1992). The parameter V_{tr} is the transverse velocity component, and can be calculated as

$$V_{tr,i} = \sqrt{(\dot{Y}_i cos(\zeta_i))^2 + (\dot{X}_i sin(\zeta_i))^2} \tag{B.4}$$

The parameter T_{il} is the thrust due to in-line velocity fluctuations found in Section B.1. The coefficient β_{tr} is then calculated using (4.12). The given thrust due to both the in-line and the transverse velocity fluctuations is then given by

$$T_a = \beta_{tr}\beta_{il}T_N = \beta_{tr}T_{il} \tag{B.5}$$

where $\beta_{tt} = 1$, $\beta_{th} = 1$ and$\beta_{tns} = 1$ from (5.1).

Appendix C

MATLAB Code

```
% Calculation of the thruster forces
function [ftx, fty] = calculate_f_thrusters(theta,
    z_dot)

global n ro

% Diameter of propeller
d = 0.076;

% Cross-coupling drag factor
K_cc = 0.25;

% Shaft speed given by each thruster on each link
RPS = [0;0;0;0;0];

% Angle of attack
zeta = [deg2rad(0);deg2rad(0);deg2rad(0);deg2rad
    (0);deg2rad(0)];

% Checks if the input is correct
```

```
19 if length(RPS)~=n
20     disp('ERROR: Dimensions of the shaft speed
           should be equal to the number of links');
21 elseif length(zeta)~=n
22     disp('ERROR: Dimensions of zeta should be
           equal to the number of links');
23 end
24
25 % The thrusters direction
26 bx = [cos(theta(1)+zeta(1));cos(theta(2)+zeta(2));
       cos(theta(3)+zeta(3));cos(theta(4)+zeta(4));cos
       (theta(5)+zeta(5))];
27 by = [sin(theta(1)+zeta(1));sin(theta(2)+zeta(2));
       sin(theta(3)+zeta(3));sin(theta(4)+zeta(4));sin
       (theta(5)+zeta(5))];
28
29 Bx = diag(bx);
30 By = diag(by);
31
32 %% In-line velocity fluctuations
33
34 % Nominal
35 K_T0 = -0.15*0.0^2 - 0.25*0.0 + 0.4;
36
37 % Actual (in-line)
38 K_T1 = -0.15*0.2^2 - 0.25*0.2 + 0.4;
39 K_T2 = -0.15*0.4^2 - 0.25*0.4 + 0.4;
40 K_T3 = -0.15*0.6^2 - 0.25*0.6 + 0.4;
41 K_T4 = -0.15*0.8^2 - 0.25*0.8 + 0.4;
42
43 % Calculates the thrust due to in-line velocity
```

```
    fluctuations by using the
% shaft speed (RPS)
T_x = zeros(n,1);
for i=1:n
    T_x(i) = sign(RPS(i))*K_T0*ro*d^4*RPS(i)^2;
end

%% Transverse velocity fluctuations
R = calculate_R_joint_global_diag(theta);
z_dot_lokal = R*z_dot;
x_dot_lokal = z_dot_lokal(1:n,1);
y_dot_lokal = z_dot_lokal(n+1:2*n,1);

% Transverse velocity component
V_tr=zeros(n,1);
for i=1:n
    V_tr(i) = sqrt((y_dot_lokal(i)*cos(zeta(i)))
        ^2+(x_dot_lokal(i)*sin(zeta(i)))^2);
end

% Thrust loss factor
beta_tr = zeros(n,1);
for i=1:n
    if T_x(i)==0
        div = 0;
    else
        div = (V_tr(i)^2)/(T_x(i));
    end
    beta_tr(i) = 1 - ro*K_cc^2*d^2*div;
end

```

```
73 % In-line and transverse velocity fluctuations
74 T_a = diag(beta_tr)*T_x;
75
76 % Forces from the thrusters, global frame
77 ftx = Bx.'*T_a;
78 fty = By.'*T_a;
79
80 end
```